A Numerical Study of Empty Nose Syndrome: an Evaluation of Nasal Aerodynamics

Eveline Løvaas Thune
University of Bergen, Department of Physics and Technology
Bergen, Norway

June 1, 2018

A thesis submitted in partial fulfilment of the requirements for the degree of *Master of Science* in the subject of Process Technology: Multiphase Systems

Acknowledgement

Firstly, I would like to thank my supervisor Prof. Pawel Kosinski at University in Bergen, he has been hugely supportive during my work with the master thesis. He consistently had a ready smile on his face and a positive attitude, and were a really easy person to go and talk to. Furthermore, he was also always ready to give me valuable and specific guidance and feed-back of the work I had done. Another person who I could not have done this without is Prof. Boris Balakin from the Western Norway University of Applied Sciences for providing me with the geometry models, and helping me with the set-up of the models. As well as for being very helpful with answering my questions about the software STAR-CCM+. I would also like to acknowledge the Empty Nose Syndrome International Association for their theoretical support, and another big thank you to Sergey Alyaev (IRIS) and Western Norway University of Applied Sciences who performed the automatic segmentation of the CT-images whitin their joint project ARIEL.

I would direct a big thank you to my classmates at the office, and then especially Sigrid and Rebecca who have made this period of my life memorable. We have shared in each others ups and downs, and have helped and supported each other well throughout the process of writing the master thesis. Not least, we have shared many good laughs together throughout the year, and I will look back on this time we have shared together with lots of fond memories.

Finally, I have to thank my parents, who are two of the most precious, valued and important people in my life. They have always been there for me, supported me in my choices, and facilitated so I could follow my dreams.

Bergen, 1. June 2018

Eveline Løvaas Thune

Abstract

Empty nose syndrome (ENS) is a rare complication of nasal surgery done to enlarge the internal nasal channels. The feeling of nasal obstruction despite patency is one of the most common symptoms among ENS patients. This study was conducted using the CFD software STAR-CCM+ to offer an analysis and visualization of airflow patterns within the nasal cavity during inhalation and exhalation. In addition, deposition of inhaled particles and clearance in the nasal cavity were studied. Five numerical models of nasal cavities from different patients were constructed. For two of the cases, the patients had confirmed ENS, other two have an obstruction in the nasal cavity, and the final one is completely healthy.

The results of the analysis showed for one ENS geometry a very low resistance during both inhalation and exhalation when compared to the other cases. Furthermore, all the geometries except the healthy one, showed a lower resistance at exhalation than at inhalation. The study on particle deposition revealed for one of the ENS geometries a low deposition ratio, which was significantly lower than for all the other geometries. Further, for the other ENS geometry showed a lower particle deposition ratio after developing ENS. Loss of nasal mucosa was suggested as a possible cause for the low particle deposition ratio, but this needs further investigation.

Nomenclature

Abbreviations

CFD	Computational Fluid Dynamics
CSA	Cross-Sectional Area
CT	Computer Tomography
ENS	Empty Nose Syndrome
FD	Finite Difference
FE	Finite Element
FV	Finite Volume
IM	Inferior Meatus
IT	Inferior Turbinates
MM	Middle Meatus
MRI	Magnetic Resonance Imaging
MT	Middle Turbinates
PIP	Point Inclusion Probability
SM	Superior Meatus
ST	Superior Turbinates

Greek letters

β	dimensionless constant	
μ	dynamic viscosity	$\mathrm{Pa} \cdot \mathrm{s} = \mathrm{kg} \cdot \mathrm{m}^{-1} \cdot \mathrm{s}^{-1}$
ω	curl of the fluid velocity	$\mathrm{rad} \cdot \mathrm{s}^{-1}$
π	constant	3.14
ρ	density	$\mathrm{kg} \cdot \mathrm{m}^{-3}$
ρ_c	continuous phase density	$\mathrm{kg} \cdot \mathrm{m}^{-3}$

Symbols

ΔP	pressure difference	Pa
$\dot{m}$	mass flow rate	$\mathrm{kg} \cdot \mathrm{s}^{-1}$

∇p	pressure gradient	$\mathrm{Pa} \cdot \mathrm{m}^{-1}$
∇	divergence	$1 \cdot \mathrm{s}^{-1}$
a	acceleration	$\mathrm{m} \cdot \mathrm{s}^{-2}$
A_p	projected area of the particle	m^2
c	mass fraction	
C_d	drag coefficient	
C_{LS}	shear lift coefficient	
c_p	specific heat	$\mathrm{J} \cdot \mathrm{kg}^{-1}\mathrm{K}^{-1}$
C_{vm}	virtual mass coefficient	
D_p	particle diameter	m
D_{H2O}	mass diffusivity of vapour in air	$\mathrm{m}^2 \cdot \mathrm{s}^{-1}$
F	force	$\mathrm{kg} \cdot \mathrm{m} \cdot \mathrm{s}^{-2}$
f	Darcy friction factor	
F_b	body forces	$\mathrm{kg} \cdot \mathrm{m} \cdot \mathrm{s}^{-2}$
F_d	drag forces	$\mathrm{kg} \cdot \mathrm{m} \cdot \mathrm{s}^{-2}$
F_g	gravity forces	$\mathrm{kg} \cdot \mathrm{m} \cdot \mathrm{s}^{-2}$
F_p	pressure gradient forces	$\mathrm{kg} \cdot \mathrm{m} \cdot \mathrm{s}^{-2}$
F_s	surface forces	$\mathrm{kg} \cdot \mathrm{m} \cdot \mathrm{s}^{-2}$
F_{LS}	shear lift forces	$\mathrm{kg} \cdot \mathrm{m} \cdot \mathrm{s}^{-2}$
F_{vm}	virtual mass forces	$\mathrm{kg} \cdot \mathrm{m} \cdot \mathrm{s}^{-2}$
k	thermal conductivity	$\mathrm{W} \cdot \mathrm{m}^{-1} \cdot \mathrm{K}^{-1}$
m	mass	kg
m_p	particle mass	kg
P	pressure	Pa
Q	volumetric flow rate	$\mathrm{ml} \cdot \mathrm{s}^{-1}$
R	resistance	$\mathrm{Pa} \cdot \mathrm{s} \cdot \mathrm{ml}^{-1}$
Re_p	particle Reynolds number	
Re_s	Reynolds number for the shear flow	
T	temperature	K

t	time	s
u_p	particle velocity	$\mathrm{m} \cdot \mathrm{s}^{-1}$
u_s	particle slip velocity	$\mathrm{m} \cdot \mathrm{s}^{-1}$
V_p	particle volume	m^3
g	gravitational acceleration	$\mathrm{m} \cdot \mathrm{s}^{-2}$
u	velocity	$\mathrm{m} \cdot \mathrm{s}^{-1}$

Contents

Chapter 1

Introduction

1.1 Background

The shape and anatomy of every nose is different. Perfect noses are rare, it is estimated that 80 % of all nasal septums, i.e. the wall which separates the left and right side of the nasal passage, are off-center. For some individuals, the septum is located too far from the nose midline so that it can cause breathing problems. This case is called a deviated septum. Sometimes, this is accompanied with enlarged turbinates (soft tissue inside the wall of the nose). They can block the airflow and further decrease a individuals ability to breathe [1].

Turbinate reduction and septoplasty also referred to as septum correction surgery, are surgeries used to correct enlarged turbinates and deviated septum, respectively. Usually these are routine surgeries, used to improve breathing problems such as sleep apnea and abnormal airflow. However, in some rare cases, patients have reported worsened breathing after their nasal passages are opened up with surgery. Other physical symptoms and even psychological symptoms may emerge, decreasing a patients overall quality of life. One such condition is called "empty nose syndrome" [1].

Empty nose syndrome is one of the least documented complications of nasal breathing [2]. It is a rare complication of nose or sinus surgery, typically after a turbinate reduction surgery. The syndrome is not a fully formally recognized health issue in the medical community yet. Most turbinate reduction and septoplasty are considered successful in improving symptoms of nasal obstruction. Therefore, many doctors regard it counterintuitive that a surgery used to expand a person's nasal passages would actually worsen their ability to breathe. As a result, when patients complain of nasal obstruction despite objective patency, it is often incorrectly assumed that the symptoms were psychosomatic [1, 3].

Ear, nose and throat specialists sometimes diagnose ENS based on a patients symptoms and by using a computer tomography (CT) to check the turbinates for damage. A characterized symptom of empty nose syndrome is a nose that feels "clogged". The treatment options for ENS patients are both surgical and non-surgical. Non-surgical treatments will not cure ENS, because it cannot restore the missing turbinates. This form of treatment is directed toward preservation and care of the remaining nasal mucosa, which is a thick layer of tissue, rich with blood vessels and central nervous systems, covering the entire inner cavities of the nose [4]. The aim of surgical procedure is to restore the inner nasal geometrical structure of the nasal passage and thereby permanently relieve the symptoms of ENS [5].

There is no clear answer about how many people in the world that have ENS, but the ENS association estimate the numbers to be in thousands. Many people undergo turbinate surgeries, for instance in France there are about 12,000 patients who undergo the surgery every year, but the exact percentage of people who develop ENS is not known [6].

1.2 Motivation and objective

As mentioned above, the precise pathogenesis of ENS is poorly understood. However, altered nasal aerodynamics is often suspected to be a major contributing factor. By applying computational fluid dynamics (CFD), a detailed examination of nasal aerodynamics can be achieved, and thus further improve our understanding of ENS. At present time, the aerodynamics for pre- and post-operative ENS patients have been numerically investigated in literature, but there is still a shortage of research on how ENS affects the functions of the nose, and especially during exhalation. Most prior CFD studies are only based on virtual turbinectomies simulated on healthy noses [7].

A motivating factor for this thesis was the lack of studies surrounding this topic, and considering how severely this syndrome affects the patient. ENS must be more researched to get a broader sense of the functional and physiological burden of obtaining ENS. Thus, this can possibly contribute to help patients in the ENS community.

This study aims to present flow patterns in the nasal cavity, and compare nasal aerodynamics during inhalation and exhalation, between geometries acquired by means of CT data from four individuals, where two have developed ENS, by using CFD software STAR-CCM+. In addition, inhaled particles deposition and clearance in the nasal cavity were studied. Currently there is almost no litterature on particle deposition in a nasal cavity, and especially if the patient has ENS. Considering the health effects of lung deposition, and in relation to estimation of toxic dose from inhaled aerosols, this topic is very important.

Chapter 2

Medical background

In order to understand the problem considered in the present work, the anatomy of the nose and some more material on empty nose syndrome are shown in this section.

2.1 Anatomy

2.1.1 Nose and nasal cavity

The anatomy of the nose differs between the different racial and ethnic groups in the world, and therefore the current description constitutes a generalization. The human nose can structurally be divided into the external and internal part. The external nose is the visible part and it includes the root between the eyes and the apex of the nose. The spanning between the root and the apex is the dorsum, also called the "bridge" of the nose. Separated by the nasal septum cartilage and located inferiorly to the apex are the nostrils, which allow air to enter the internal part of the nose that is the nasal cavity [8].

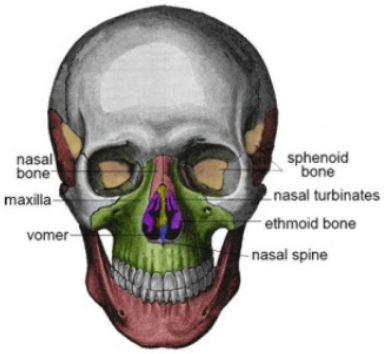

Figure 2.1: Anatomy of the nose, showing the nasal cavity and the supporting facial bones [8].

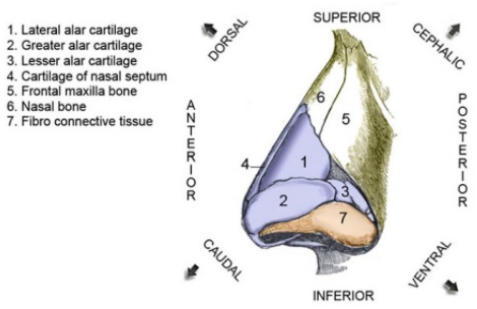

Figure 2.2: A sideways view of the external nose showing the cartilage and bone structure [8].

The skeleton of the external part of the nose is composed of both bony and cartilage components. The bony element, comprised of the nasal bones, maxillae and frontal bone are displayed in Figure 2.1 showing their position. Figure 2.2 shows the cartilaginous components.

The nasal cavity, also referred to as the breathing passage, lies just behind the two nostrils and forms the interiors of the nose. It extends from the external opening, the nostrils, to the upper section of the throat labeled the nasopharynx, where it joins

the remainder of the respiratory system [9]. The walls in the cavity are lined with respiratory mucosa. The internal structure of the nasal cavity is shown in Figure 2.3. There are three passageways; superior, middle, and inferior meatus, formed by the superior, middle and inferior nasal turbinates that projects medially into the nasal cavity [8].

The turbinates and the nasal septum

Since turbinate reduction and septum correction surgery are a focal point of the subject of ENS, they are described in detail in this section.

Turbinates are also referred as nasal conchae because of the likeness to a conch seashell. They are shaped as a long, narrow and curly bone shelf with an outer lining of mucous membrane [6]. Figure 2.3 shows a lateral view of a human right nasal cavity.

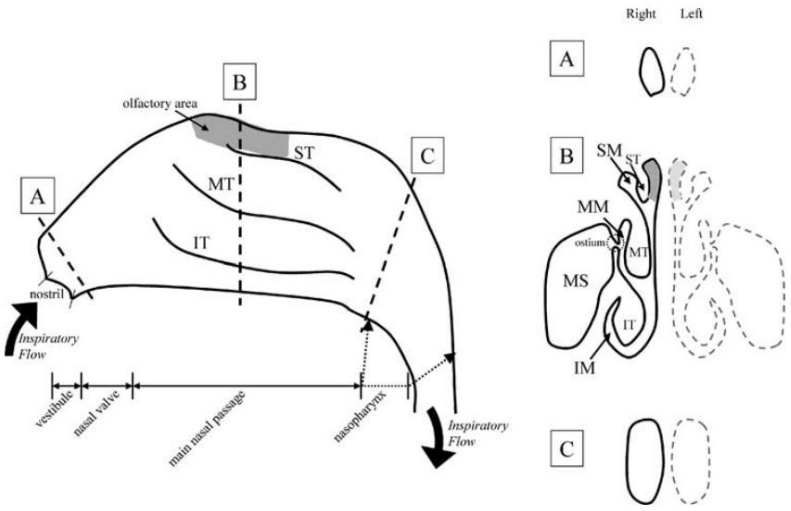

Figure 2.3: A, B and C on the right part of the figure correspond to three different nasal cross-sections represented on the left. IT, MT and ST refer to inferior, middle and superior turbinates. IM, MM, and SM refers to inferior, middle, and superior meatuses. MS refers to the maxillary sinus [10].

Confined between the nostrils is the nasal septum, a mucous membrane lining the entire septum on either side. The center part of the septum is made of bone and cartilage [11]. Ideally, the septum would be a straight wall, but nearly everyone has some degree of deviated nasal septum. The degree of the deviation of the septum, as well as the anatomy of the side wall of the nose can, as mentioned in the introduction, sometimes be so displaced that it can result in various degree of blockage of the nasal passages [12]. Figure 2.4 displays the shape and location of the septum as well as the turbinates.

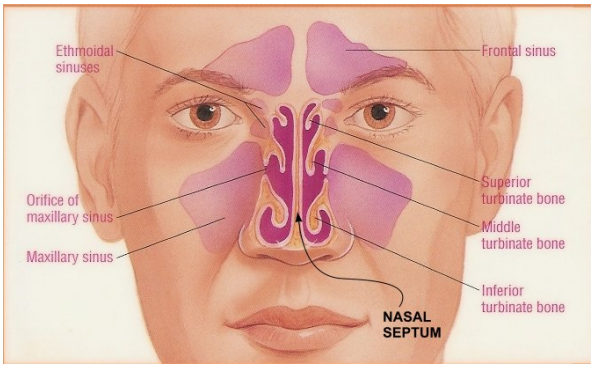

Figure 2.4: An ideal midline nasal septum with all three turbinates [13].

2.2 Physiology

The nose and its internal nasal cavity warms and humidifies the inhaled air, and the mucosa on the walls traps any inhaled particulates, thus filtering the inhaled air. Dust and bacteria are examples of particulates. Another function is speech resonance [8].

The mucosa surrounding the turbinates is subject to tremendous elevating capabilities of nasal congestion and decongestion, in response to the climatic conditions and changing needs of the body. This affects the flow resistance due to the airway passages narrowing or expanding [8]. The inferior and middle turbinate (IT and MT) are respectively, the largest and second largest in size. They are the most important ones in terms of directing and controlling airflow, and maintaining healthy nasal functions. The turbinates also increase the surface area of the nasal cavity, thus contributing to accelerated warming and humidification of air as it passes [14]. The superior turbinates have smaller structures, and are connected to the middle turbinates by nerve-endings. They serve to protect the olfactory bulbs at the roof of the nose (just under the bone barrier between the brain and the nasal cavities) and harbors some smell receptors [15].

The septum allows the inhaled air as it flows through the nostrils to go directly from the tip of the nose into the back of the nose, and into the lungs. Without the septum, the air might not find a direct transit into the lungs, because the turbulence might interfere [11].

2.3 Empty nose syndrome

Patients with ENS, generally have been subjected to a surgically resection of the IT, but MT resection or even the presence of normal turbinate tissue and intranasal volume are also associated with ENS. Nevertheless, in all cases of ENS, patients have had some type of turbinate procedure carried out during their lifetimes [16]. Chhabra et al. [16] estimates that approximately 20 % of patients with IT resection will develop ENS and that a greater percentage suffers from at least dryness. Figures 2.5 and 2.6 show examples of IT- and MT resections, respectively.

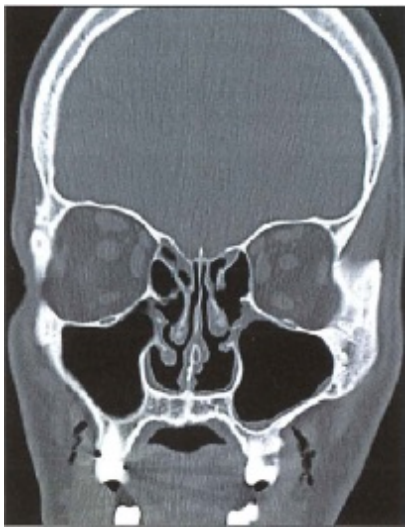

Figure 2.5: A CT scan of a patient with ENS-IT [16].

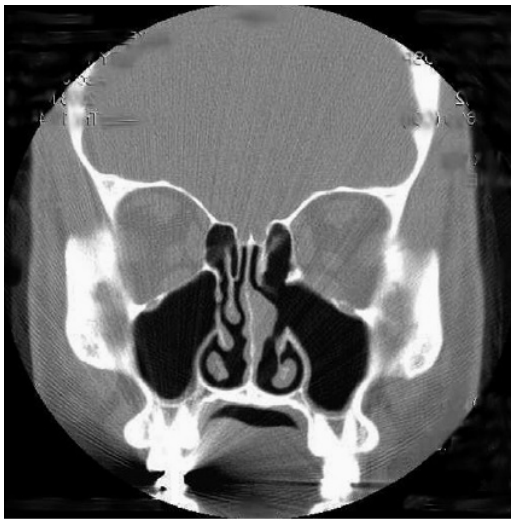

Figure 2.6: A CT scan of a patient with ENS-MT [17].

As mentioned some patients that have undergone a complete turbinate removal will not develop ENS, while others will develop ENS symptoms with a partially removed turbinate. Symptom severity and how much it will affect the patients quality of life differs from case to case. In the most severe cases, patients report a constant sense of suffocation. It is also common that ENS can lead to a comorbid depression. ENS can develop within weeks, months or years following turbinate surgery. A key factor in the development of ENS seems to be the loss of mucosa, which leads to an alternate airflow and a lacking in sensation [17].

It is not well understood why ENS-IT is the most common subtype, but it may be a result of the IT physiologic function. ITs act as pressure valves and are responsible for adjusting the amount of nasal airflow, and also for increasing flow velocity upwards, see Figure 3.1. The ITs direct nearly 60 % of airflow upward through the MT (50 %) and ST (10 %). MT resection is considered within the standard care of sinonasal surgery, but ENS-MT is a rare syndrome, often involving pain associated with breathing. ENS-both is another subtype, it refers to patients who have had both an IT and a MT resection of the tissue. This is the most severe form of ENS, and the patients symptoms are often disabling. In many cases the depression rates are higher with this subtype [16, 17].

Chapter 3

Literature study

Detailed in vivo studies of nasal air conditioning are prevented due to the intricate 3D structure and poor accessibility of the nasal cavity. Therefore, a variety of experimental and numerical models have been used for the analysis of airflow patterns in the nasal cavity [18]. Some of the studies are presented in this chapter.

3.1 Studies on airflow using CFD

Hildebrandt et al. [19] used CFD with a symptom-free subject and a symptomatic patient. They studied the features of the intranasal flow field that might be of special clinical relevance, such as: pressure, nasal resistance and flow field. In addition, changes before and after surgery were investigated. The symptomatic patient suffered from a chronic blocked nose without sensing a predominant side, caused by a deviated septum within the isthmus area, which is the posterior segment of the nasal valve region, shown in Figure 2.3.

The result of the numerical simulation showed particularly an "inhalation jet" from the isthmus nasi into the middle meatus in the symptom-free subject. In addition, a relatively high spatial disparity of the flow velocity was seen in the nasal cavity. In comparison, the exhalation phase showed a more homogenous velocity distribution. For the distribution of total pressure, a boundary of the nasal vestibulum from the further posterior nasal cavity was clearly shown. This result is supported by the fact that at isthmus nasi, up to 80 % of the total inhalation nasal resistance originates. Further, certain changes of flow simulation before and after surgery was of special interest in the symptomatic case. Because of the septoplasty, i.e reconstruction of the deviated septum, a decline of the flow space constriction in the anterior part of the left nasal cavity were obtained. This resulted in a shifting of flow distribution between the nostrils, and the inhalation resistance increased. Not only the resistance on the right side but also the pressure drop or resistance of the entire nasal cavity increased.

Zhu et al. [20] evaluated the effects that a deviation of the external nose has on the nasal airflow patterns by use of CFD simulations. Four typical subjects were chosen for model reconstruction based on CT images of three different shaped deviated and undeviated noses. Flow rates of 167 and 500 ml/s were carried out in the models. In all the deviated noses the shape of the anterior nasal roof was found to be collapsed on one side of the nasal airways. A considerably larger nasal resistance was found in the cavities in the deviated noses compared to healthy nasal cavity, while the internal blockage of the airway along the turbinates further increased it. However, in all the models, the resistance at flow rate 500 ml/s was considerably larger than at 167 ml/s.

Riazuddin et al. [21] CFD study investigated the flow mechanisms in the nasal cavity for the inhalation phase and exhalation phase. Variations in flow patterns and flow features such as pressure drop, velocity in the left and right cavity were observed. The flow resistance during inhalation was greater compared to the exhalation phase. It was also observed that the resistance curve in the female subject was much steeper than those of the male subjects. This may be attributed to the anatomical differences.

3.2 Numerical studies on ENS

Balakin et al. [2] gave an overall aerodynamic CFD-description for a pre- and post-operative geometry, where the patient was diagnosed with ENS post-operation. Their aim was to compare and analyze the deviation of airflow patterns and nasal microclimate from healthy benchmarks. Their analysis revealed a 53 % reduction of the nasal flow resistance in the post-operative case. In addition, the ENS geometry displayed radical re-distribution of the nasal airflow, as well as dryer and colder nasal microclimate.

Li et al. [7] studied nasal aerodynamics and trigeminal sensory factors in six patients diagnosed with ENS. Three of them had pre- and post-inferior turbinate reduction CT scans, which allowed for comparison of their nasal aerodynamics through CFD. Post-surgical reductions in nasal resistance were observed and were detected significantly lower than normal. Paradoxically for all ENS patients, the analysis showed that IT reduction did not draw more airflow to the airway surrounding the ITs, but rather resulted in reduced nasal airflow intensity and air-mucosal interactions (inferior region flow percentage reduced from $35.7\% \pm 15.9\%$ to post-surgery $17.7\% \pm 15.7\%$).

In another study done by Li et al. [22] individual CT-based CFD was applied to 27 ENS patients to simulate their nasal aerodynamics and compared them to 42 healthy controls. It is the first CFD examination of nasal aerodynamics in a large cohort of ENS patients. The patients symptoms were confirmed with ENS 6-item Questionaire, 22-item Sino-Nasal Outcome Test and Nasal Obstruction Symptom Evaluation scores. The results of the study revealed for the ENS patients a $\sim 25.7\%$ lower nasal resistance and a $\sim$ 2.8 times cross-sectional compared to the healthy controls. Despite inferior turbinate reductions, the CFD analysis demonstrated that ENS patients had an increased airflow. The airflow was concentrated in the middle meatus region ($66.5\% \pm 18.3\%$) and left majority of the IT region without air movement, compared to the healthy controls ($49.9\% \pm 15.1\%$). The healthy patients had uniformly distributed streamlines throughout both the IT and MT region. This is shown in Figure 3.1. Further, the symptoms score of ENS 6-item Questionaire indicated that less air-mucosal stimulations resulted in worse symptom scores.

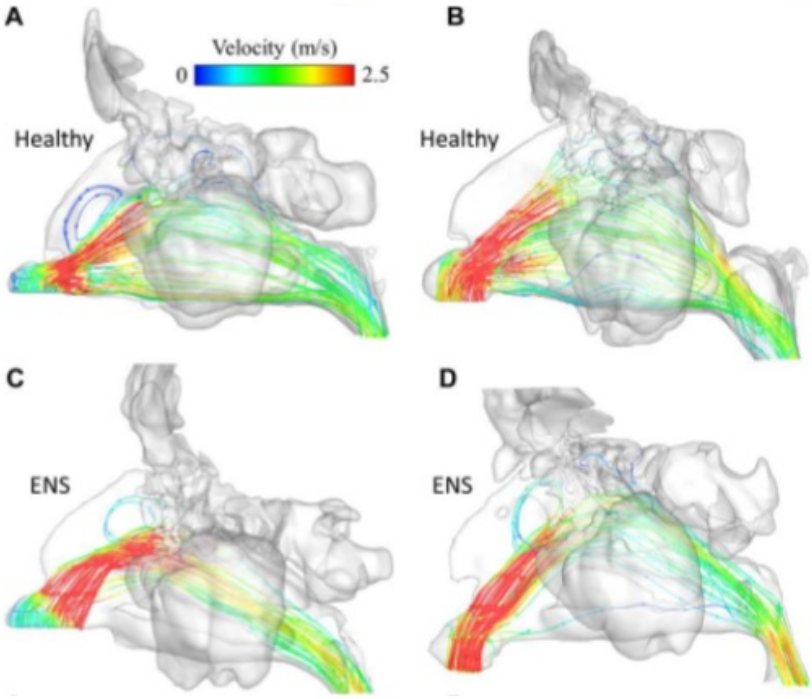

Figure 3.1: Streamline patterns of two healthy patients (A,B) and two ENS patients (C,D) [22].

Di et al. [23] investigated the nasal aerodynamics features of ENS and explored the role of aerodynamic changes on the pathogenesis of ENS. Seven sinonasal models were numerically constructed, based on CT images of seven healthy male adults. Bilateral radical inferior/middle turbinectomy were numerically performed to mimic the typical nasal structures of ENS-IT and ENS-MT. The results showed for ENS-MT a similarity in streamlines, air flux distribution and wall shear stress distribution to those of the normal structures. However, nasal resistances decreased. Like the study done by Li et al. [22], the ENS-IT models showed that streamlines were less organized near the bottom wall.

Wexler et al. [24] studied the aerodynamic effects of a one-sided inferior turbinate reduction by use of CFD methods. The model was constructed from magnetic resonance imaging (MRI) data of a healthy man, where they modelled a circumferential removal of 2 mm of soft tissue bulk along the length of the left IT. The results showed a broad reduction of pressure along the nasal airway, including the regions distant from the IT vicinity. Nearly 60 % decline in pressure was calculated at the proximal valve region. Further, conservative IT reduction produces marked changes in airspeed and relative airflow distribution throughout the nasal passage, where the results showed a regional relative airflow.

3.3 Studies involving deposition of aerosols particles

Cheng et al. [25] examined nasal deposition of ultrafine particles in human volunteers and its relationship to airway geometry. All the subjects were healthy adult men and nonsmoking. The test method was that each subject held his breath for 30-60 sec, during which time, the aerosol was drawn through the nasal airway and exhausted through a mouth tube. The deposition efficiency in the nasal airway was calculated considering particle losses in the mask, mouth tube, and transport lines. The nasal deposition varied widely among the four subjects. Cheng et al. suggested that the deposition can be correlated based on specific parameters like cross-sectional area, mean perimeter and total surface area. This correlation indicates a higher nasal deposition for a person with a smaller cross-sectional area, larger surface area, and a larger perimeter.

Gradon et al. [26] studied filtration of ultrafine particles in the nasal cavity, obtained from a simulation experiment in a cast of human oropharynx. They found that during normal breathing rate the inhalation deposition efficiency of particles of diameter 0.001 μ in nose and mouth were respectively 28.5 % and 16.5 %. These deposition fractions rapidly decreased to 0.1 % and 0.05 % for particles of diameter 0.1 μm. They state further that for particles with a larger diameter than 0.5 μm is the geometry of the nasal passageway is of importance. In addition, the diffusional deposition of aerosol particles in the airways becomes significant when the particle diameter is smaller than 0.01 μm.

The right passageway in a nasal cavity to an adult male were numerically investigated by Shanley et al. [27]. The model was constructed from MRI scans. Diluted, uniform concentrations of inertial ($1\mu m \leq d_p \leq 10\mu m$) particles were released at the nostril. The study showed that deposition efficiency increased with particle size and volumetric flow rate.

Schroeter et al. [28] studied localized deposition of inhaled particles in human nasal passages. A CFD model of nasal airflow were used, and the nasal valve, turbinates, and olfactory region were defined in the model. As a result particles depositing in these regions could be identified and correlated with their release positions on the nostril surfaces. The subject was a healthy adult male, and the geometry of the nasal passage was formed from MRI scan tracings. When the spherical particles were released from the nostrils, they ranged in size from 5 to 50 μm. The volumetric flow rates were 7.5, 15 and 30 L/min, and the deposition sites and particle trajectories were calculated for a steady-state inhalation airflow. When plotted against impaction parameter, deposition efficiencies in the nasal valve, turbinates and olfactory region exhibited maximum values of 53 %, 20 %, and 3 %, respectively.

By taking all the studies into consideration, research on nasal aerodynamics in the nasal cavity of patients with ENS at exhalation have not yet been conducted. Furthermore, no studies have been done on particle deposition and clearance in patients with ENS or on patients with structural obstructions in the nasal cavity. This is an important area to study because of the health risk the lung deposition poses. Therefore the objective of this thesis was to investigate these issues.

Chapter 4

Fundamentals of fluid dynamics

When trying to predict how the airflow behaves in the nasal passage during ENS, the fluid flow equations and the equations of motion must be solved. In this chapter, an introduction of the basic principles used in the numerical simulation process is outlined.

CFD is a research tool that helps to interpret and understand the results of theory and experiment. One significant advantage of using CFD compared to other commonly used techniques, such as experimental studies, is the higher degree of information obtained from numerical simulations. CFD uses computers to solve integral and partial differential equations, to extract solutions as a function of position and time in a computational domain. CFD is based on the fundamental equations governing fluid dynamics: the continuity, momentum, and energy equation. The equations are based on the conservation law of fluid physical properties [29]:

- Mass is conserved.
- Momentum balance (Newton's second law).
- Energy is conserved.

These principles state that mass, momentum and energy in a closed system are stable constants.

For the continuous fluid there are four different flow models: a finite control volume fixed in space with the fluid moving through it, a finite control volume moving with the fluid, an infinitesimal fluid element fixed in space with the fluid moving through it and an infinitesimal fluid element moving along a streamline in the fluid. Each model of the flow leads to a particular form of the governing equation, either in conservation or non-conservation form. In this study the finite control volume fixed in place with fluid moving through it applies [29].

The fundamental equations that describes viscous flow are called the Navier-Stokes equations. For the case when a flow is inviscid, these equations reduce to the Euler equations. The physical domain of the problem in this research is the 3D inner cavity of the nose with given inlet and outlet cross-sections. It is assumed that the humid air flow in the nasal channels is incompressible and laminar with constant viscosity and thermal conductivity. Inhaled air flow through the nasal cavity are controlled by the equations for conservation of mass, momentum, and energy. They are shown in the following sections.

4.1 Continuity equation

The basic principle of conservation of mass states that matter may neither be created nor destroyed, meaning for any element of fluid:

Rate of mass accumulation	=	Rate of mass flow in	-	Rate of mass flow out.

In other words:

$$0 = \sum_{in} \dot{m} - \sum_{out} \dot{m}.$$

In this research the density ρ is constant, independent of space and time. The continuity equation is therefore reduced to [2]:

$$\nabla \cdot \overrightarrow{u} = 0, \tag{4.1}$$

where $\overrightarrow{u}$ is the velocity of the air-vapour mixture.

4.2 Momentum equation

The momentum equation is based on the Newton's second law of motion. The law states that the sum of forces that act on a control volume equals its mass times the acceleration of the element:

$$\sum \overrightarrow{F} = m\overrightarrow{a}. \tag{4.2}$$

The basic concept of the momentum equation is:

Rate of momentum accumulation	=	Rate of momentum entering	-	Rate of momentum leaving	+	Sum of forces acting on the system.

There are two main sources of the force acting on a fluid element [29]:

1. *Body forces*, act at a distance and directly on the volumetric mass of the fluid element. Examples are gravitational, electric, and magnetic forces.

2. *Surface forces*, act directly on the surface of the fluid element and we can distinguish between two types. The first one is the pressure force involves the total pressure acting on the fluid element by the outside surrounding fluid. The second one is the viscous force which includes the shear and normal stress distributions acting on the surface and the friction between the outside fluid.

The momentum equation that applies for this thesis is [2]:

$$\rho(\overrightarrow{u} \cdot \nabla)\overrightarrow{u} = -\nabla p + \mu\nabla^2\overrightarrow{u}, \tag{4.3}$$

where p is the pressure, μ is the dynamic viscosity and ∇ is the divergence.

4.3 Energy equation

The energy equation is based on the physical principle of energy conservation, which is the first law of thermodynamics. When applied to a fluid element model moving with the flow, the law states that:

Rate of change of energy inside fluid element	=	Net flux of heat into element	+	Rate of work done on element due to body and surface forces.

In other words: energy is conserved in an isolated system. Therefore, the amount of energy entering the control volume must equal the amount of energy leaving it. Thus, the rate of change of energy in the control volume is equal to the net rate of heat added to the fluid element plus the net rate of work done by body and surface forces on the fluid element. The energy term consists of the fluid energy per unit mass, whereas the net rate of heat added is based on Fouriers heat conduction equation. The rate of work done by the body force consists of the force, multiplied by the component of velocity in the direction of the force [8]. Hence the energy equation is [2]:

$$(\vec{u} \cdot \nabla)T = \frac{k\rho}{c_p}\nabla^2 T, \tag{4.4}$$

where T is the temperature, k is the thermal conductivity and c_p is the specific heat.

4.4 Transport equation for moisture

Diffusion is a molecular transport process, where the corresponding physical properties are transported by the movement of the molecules in the gas. In other words: transfer or movement of individual molecules through a fluid by means of random, individual movements of the molecules [30]. In this thesis there is molecular diffusion in the air-vapour mixture, and the evolution of vapour in the system is given by a transport equation for the moisture mass fraction c_{H20} [2]:

$$(\vec{u} \cdot \nabla)c_{H_20} = D_{H2O}\nabla^2 c_{H20}, \tag{4.5}$$

where D_{H2O} is the mass diffusivity of vapour in air.

4.5 Physical boundary conditions

Although the given equations above govern the flow of a fluid through various kinds of geometry, the flow fields are quite different for each case. The reason for the difference lies with the boundary conditions. The boundary conditions determine the particular solutions to be acquired from the governing equations. Therefore, for the numerical solutions to be accurate it is important to apply certain physical boundary conditions on the particular geometric surface. In CFD this is of significance because any numerical solution of the governing flow equations needs a good numerical representation of the proper boundary conditions [29].

In this study the boundary conditions on the surface of the nose geometry need to be specified. This kind of boundaries are physical solid boundaries. Further, the inlet and outlet are considered open boundaries that also need individual specifications.

4.6 Discretization

Discretization is the process where a closed-form mathematical expression is transformed into discrete counterparts. Examples on such expression are functions, a differential or integral equation involving functions. All of which are viewed as having an infinite continuum of values throughout some domain. When they are approximated by analogous expressions prescribing values at only a finite number of discrete points or volumes in the domain, it is said to be discretized.

The technique is used to divide a domain into grid points, as illustrated in Figure 4.1. Numerical solutions can only give answers at these grid points. To solve equations at these points, discretization is necessary. The step of discretization is usually carried out as a first step toward making the equations suitable for numerical evaluation [29].

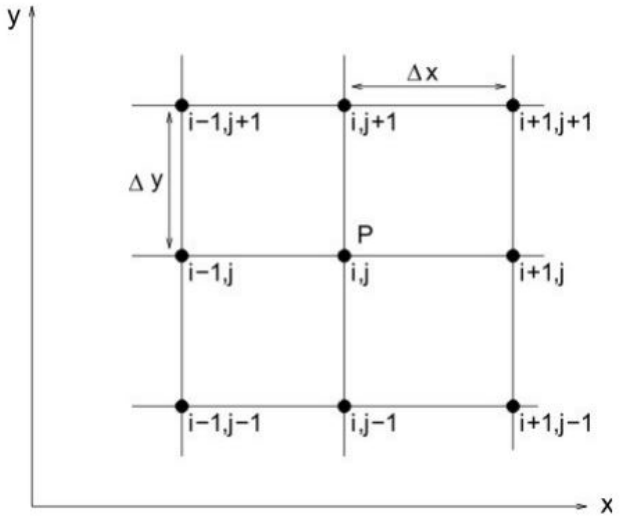

Figure 4.1: Grid points in the xy-plane [29].

There are several methods of discretization, but the most common are finite difference (FD), finite volume (FV) and finite element (FE). STAR-CCM+ supports both FV and FE solutions method. In this thesis the finite volume method is applied: STAR-CCM+ uses discretization methods to transform the mathematical model into a set of discrete algebraic equations. This transformation involves discretizing the governing equations in space and time. The resulting linear equations can then be solved using numerical techniques [31].

In the FV method, the solution domain is divided into a finite number of small cells. Discrete versions of the integral form of the continuum transport equations are applied to each control volume. The goal is to obtain a set of linear algebraic

equations, corresponding to the number of cells in the grid is the total number of unknowns in each equation system. The resulting linear equations are then solved with an algebraic multigrid solver. In case the equations are non-linear, iterative techniques that rely on appropriate linearization strategies must be employed [31].

4.7 Generation of computational mesh

As stated above, the arrangement of discrete points throughout the domain is defined as grid or mesh. To execute a numerical analysis, the solution domain is split into multiple sub-domains, which are called cells. A mesh can be viewed as several smaller cells that overlays the entire geometry domain [32]. To obtain a reliable computational solution, generation of quality mesh is of extreme importance. A good quality mesh improves numerical stability, and increases the probability of achieving a reliable solution [8].

The set of fundamental mathematical equations that represent the flow physics are in general applied to each cell. These equations calculate the changes in each cell within the entire domain geometry, afterwards they are solved to generate the corresponding discrete values of the flow-field variables such as velocity, pressure and humidity [8]. The only possible way to solve the mathematical model are under the assumption of linearity. Thus, one needs to ensure that all the variables one wishes to solve for, can be expected to be linear within each cell. In regions that are highly critical to the simulation results, a finer mesh is needed to make sure of the accuracy of the simulation. Encountered failures of the simulation are often based on errors on mesh structure. The reason might be because the mesh is too coarse and it does not cover all the effects that happen in the single element one by one, but instead cover multiple effects. This can be changed by applying finer mesh [32].

There are two types of mesh, structured and unstructured. Unstructured mesh is used with complex geometries that do not fit exactly in the Cartesian coordinates. An unstructed mesh could be constructed to fill the interior curvilinear geometries, and the lack of structure of the cells makes it highly suitable for the complex 3D models used in this thesis. In the software STAR-CCM+, several meshing models can be chosen to generate a grid suitable for various geometries and applications. The meshing models used in this thesis are described in Section 6.3 and Figures 6.5 6.6 show the applied mesh models.

4.8 Residual plot and convergence

In STAR-CCM+ a residual plot is created automatically within every simulation, the plot are useful to monitor the convergence of a solution. Convergence is important in computational analysis, because the numerical solution goes through an iterative scheme where results are obtained by the reduction of errors among the previous steps. The difference between the last two steps specifies the error. When the absolute error decreases, the accuracy of the result increases, which means that the result converges towards a steady-state condition [31, 32].

Chapter 5

Modelling multiphase flow

When studying the deposition of particles in the nasal cavity a comprehension of the topic of multiphase flow is necessary.

5.1 Multiphase flows

A multiphase flow refers to any fluid flow with more than one phase or component present. A phase pertains to the solid, liquid or gas state of the matter. The solid phase is in the form of particles, which are carried along in the flow, and the movement of the solid depends on the size of the individual elements and on the motion of the associated fluids. The liquid can constitute two different phases, a continuous phase containing dispersed elements of solids, gases or other liquids, or discontinuous in the form of drops suspended in a gas phase or in another liquid phase. As a fluid, a gas has the same properties as a liquid in its response to forces. However, in comparison to liquids and solids it is compressible when the Mach number is low [33, 34].

As mention in the introduction to the chapter, the models accompanying particle deposition in this study is a multiphase flow. There are different types of multiphase flow, it can be subdivided into four categories according to the state of the different phases or components: gas-liquid, gas-solid, liquid-solid and three-phase flow. In this thesis we have both a single-phase multicomponent flow and gas-liquid multiphase flow. The air flow represents a single phase multicomponent system because it consists of a mixture of various gases and water vapour. About different flows, it is important to mention the difference between a multicomponent and multiphase flow. A multicomponent flow is a flow consisting of two or more chemical species mixed together into a single phase at molecular level. In this thesis, the gas components that represents the gas mixture are air and water with a known viscosity, thermal conductivity and specific heat. The gas phase represents the carrier phase, which is the continuous phase, and the liquid particles represent the dispersed phase [33].

Eulerian-Lagrangian

Lagrangian numerical methods in combination with Eulerian numerical methods are widely used to simulate multiphase flows. The particles that constitute the dispersed phase are represented in a Lagrangian approach, the model solves the equation of motion for the representative particles as they pass through the system. The continuous phase is expressed in the Eulerian form, which means the model solves the Navier-Stokes equations for the fluid flow. The equations are altered to take into

account the presence of the dispersed phase.

The Eulerian-Lagrangian approach is best suited for systems that consist mainly of a single continuous phase transporting a relatively small volume of discrete particles. In this thesis, this approach is used to examine particle deposition in the nasal cavity.

5.2 Basic equations

As stated above, in multiphase flow the flow consists of a continuous phase, and one or more dispersed phases. In this thesis, there is only one dispersed phase in the form of liquid particles. The forces mentioned in this section are within the Eulerian-Lagrangian approach. Their respective equations are from the STAR-CCM+ user guide [31].

Modelling the continuous phase

The gas components represent the continuous phase solved with the Eulerian approach based on equations (4.1) and (4.3). A term is added to the momentum equation: resulting from drag, lift and pressure gradient forces.

Modelling the dispersed phase

The Lagrangian model solves the equation of motion for the liquid particles as they pass through the nasal cavity. The equations for the applied models for the forces of drag, shear lift, gradient pressure, virtual mass and gravity are presented in this section.

The momentum equation for a material particle of mass m_p is:

$$m_p \frac{d\overrightarrow{u}_p}{dt} = \overrightarrow{F}_s + \overrightarrow{F}_b, \tag{5.1}$$

where m_p is the particle mass, $\overrightarrow{u}_p$ is the instantaneous particle velocity, and $\overrightarrow{F}_s$ represents the forces that act on the surface of the particle:

$$\overrightarrow{F}_s = \overrightarrow{F}_d + \overrightarrow{F}_p + \overrightarrow{F}_{vm} + \overrightarrow{F}_{LS}. \tag{5.2}$$

$\overrightarrow{F}_b$ represents the body forces:

$$\overrightarrow{F}_b = \overrightarrow{F}_g, \tag{5.3}$$

where $\overrightarrow{F}_d$ is the drag force, $\overrightarrow{F}_p$ is the pressure gradient force, $\overrightarrow{F}_{vm}$ the virtual mass force, $\overrightarrow{F}_g$ is the gravity force and $\overrightarrow{F}_{LS}$ is the shear lift force.

Thus:

$$m_p \frac{d\overrightarrow{u}_p}{dt} = \overrightarrow{F}_d + \overrightarrow{F}_p + \overrightarrow{F}_{vm} + \overrightarrow{F}_g + \overrightarrow{F}_{LS}. \tag{5.4}$$

The drag force

The force in the direction of a flow, exerted by the fluid on a moving object, is called drag. Drag is the net force in the direction of flow due to pressure and shear stress forces on the surface of the object. The drag force can be expressed as:

$$\overrightarrow{F}_d = \frac{1}{2} C_d \rho_c A_p |\overrightarrow{u}_s| \overrightarrow{u}_s, \tag{5.5}$$

where C_d is the drag coefficient of the particle, ρ_c is the density of the continuous phase, $\overrightarrow{u}_s = \overrightarrow{u} - \overrightarrow{u}_p$ is the particle slip velocity and A_p is the projected area of the particle.

The drag force model calculates the force on a material particle in the dispersed phase due to its velocity relative to the continuous phase. The drag coefficient is used to formulate the drag force, and it is a function of the small-scale flow features around the individual particles. The usual practice is to obtain the drag coefficient from correlations, since the features are impractical to resolve spatially. These correlations differ according to the nature of the dispersed phase. The selected method in STAR-CCM+ used for defining the drag coefficient is the Schiller-Naumann correlation:

$$C_d = \begin{cases} \frac{24}{Re_p}(1 + 0.15 Re_p^{0.687}) & Re_p \leq 10^3 \\ \\ 0.44 & Re_p > 10^3, \end{cases} \tag{5.6}$$

where Re_p is the particle Reynolds number, defined as:

$$Re_p \equiv \frac{\rho |\overrightarrow{u}_s| D_p}{\mu}. \tag{5.7}$$

In the above, D_p is the particle diameter. This correlation is only available when the continuous phase is viscous.

The pressure gradient force

The pressure gradient force occurs when there is a difference in pressure across a surface. The equation is expressed as:

$$\overrightarrow{F}_p = -V_p \nabla p, \tag{5.8}$$

where V_p is the particle volume, and ∇p is the gradient of the pressure in the continuous phase.

The shear lift force

The particle shear lift force model applies to a particle moving relative to a fluid, where there is a velocity gradient in the fluid perpendicular to the relative motion. The spin lift force model calculates the force acting on a spinning particle moving in a fluid. STAR-CCM+ calculates the spin lift force using a particle lift coefficient. The three-dimensional version of the shear lift force equation is:

$$\overrightarrow{F}_{LS} = C_{LS} \frac{\rho \pi}{8} D^3 (\overrightarrow{u}_s \times \overrightarrow{\omega}), \tag{5.9}$$

where $\overrightarrow{\omega} = \nabla \times \overrightarrow{u}$ is the curl of the fluid velocity and C_{LS} is the shear lift coefficient.

The defined lift coefficient in this thesis is based on the Sommerfeld method:

$$C_{LS} = \frac{4.1126}{Re_s^{0.5}} f Re_p, Re_s, \tag{5.10}$$

where:

$$f Re_p, Re_s = \begin{cases} (1 - 0.3314\beta^{0.5})e^{-0.1 Re_p} + 0.3314\beta^{0.5}, & (Re_p \leq 40) \\ 0.0524(\beta Re_p)^{0.5}, & (Re_p > 40) \end{cases} \tag{5.11}$$

and

$$\beta = 0.5\frac{Re_s}{Re_p}, \tag{5.12}$$

where Re_S is the Reynolds number for shear flow, $Re_S = \frac{\rho D^2 |\overrightarrow{\omega}|}{\mu}$, and f is the Darcy friction factor.

The virtual mass force and gravity force

The virtual mass model accounts for the additional resistance that is experienced by a particle accelerating through a fluid. This resistance can be significant when the particle has a density that is comparable to, or much smaller than, the surrounding fluid.

The equation for the virtual mass force is defined as:

$$\overrightarrow{F}_{vm} = C_{vm}\rho_c V_p(\frac{D\overrightarrow{u}}{Dt} - \frac{d\overrightarrow{u}_p}{dt}), \tag{5.13}$$

where C_{vm} is the virtual mass coefficient, and the operator $\frac{D}{Dt}$ is the material derivative. The default value of 0.5 for this coefficient is for a sphere in a uniform, inviscid, incompressible flow.

The gravity force equation is:

$$\overrightarrow{F}_g = m_p \overrightarrow{g}, \tag{5.14}$$

where $\overrightarrow{g}$ is the gravitational acceleration factor.

Chapter 6

Methodology

This chapter gives a description of the geometries and mesh used in all the simulations. Additionally, the physics models, solvers and boundary conditions required to compute the problem are shown.

6.1 CT images and geometries

For construction of a computational model of the human nasal cavity, medical CT images were obtained in this research. 3D models of nasal configurations were obtained using an automatical segmenter ARIEL developed by IRIS and Western Norway University of Applied Sciences.

The geometry used in the simulations originates from CT-data for four different patients, one patient has CT-data for both pre- and post-operative case. This resulted in five different 3D-models. All of the patients are Caucasians, and some more background info about the patients is shown below:

- Patient 1 and 2 is a 26-year old female with a nasal obstruction referred as patient 1 that was operated so that ENS developed is referred as patient 2.
- Patient 3 is a 51-year old man with ENS.
- Patient 4 is a 36-year old man with nasal polyposis.
- Patient 5 is a healthy 30-year old woman.

From this point on, patient 1 will be referred to as geometry 1, patient 2 as geometry 2, etc.

The segmented data obtained from ARIEL was imported into STAR-CCM+, and formed the basis for the models. Figure 6.1 illustrates an imported geometry for geometry 1 and 2 including the paranasal sinuses. The figure also exhibits the two nostrils as inlets and the nasopharynx as an outlet for the inhalation. At exhalation we investigate the opposite situation, i.e. the nasopharynx becomes the inlet. Figures 6.2 and 6.3 illustrates the imported geometry for the rest of the geometries. In each geometry 12 coronal cross-sections were defined along the nasal passage, see Figure 6.4.

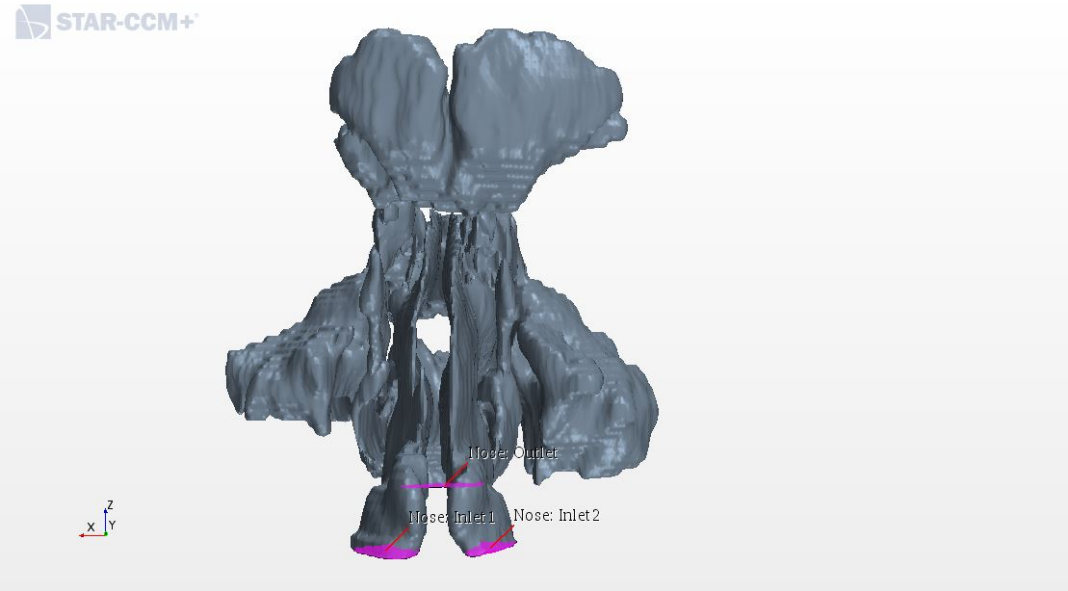

(a) Geometry 1.

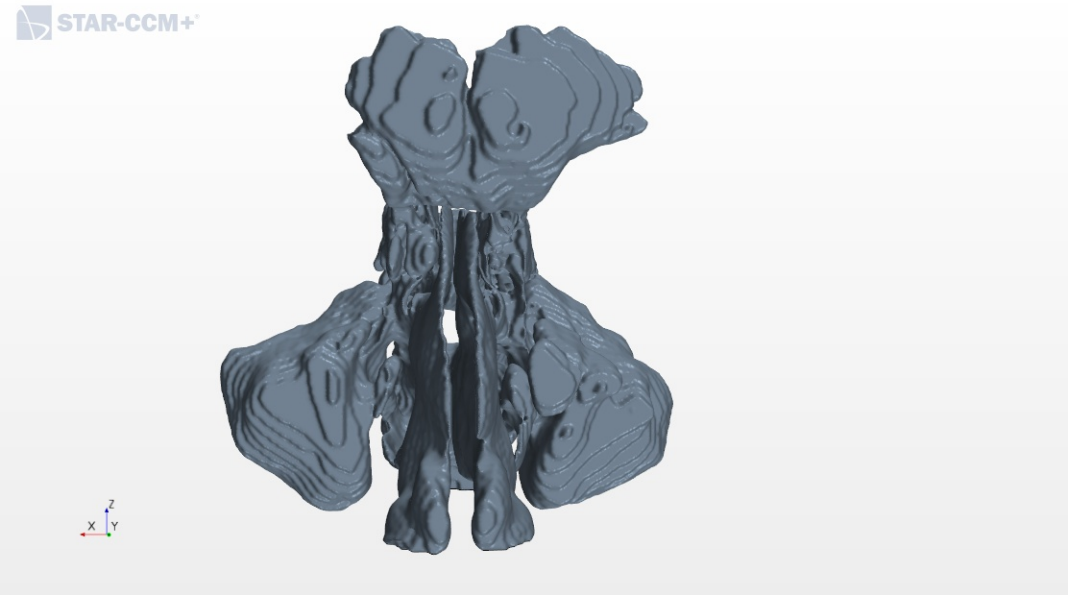

(b) Geometry 2.

Figure 6.1: Front view of the nasal channels.

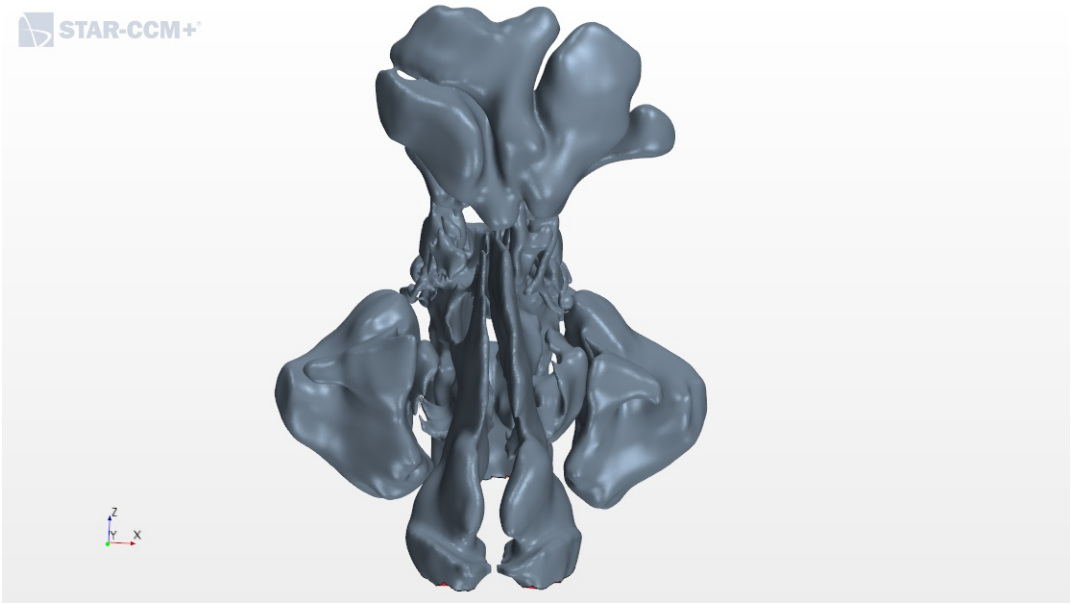

(a) Geometry 3.

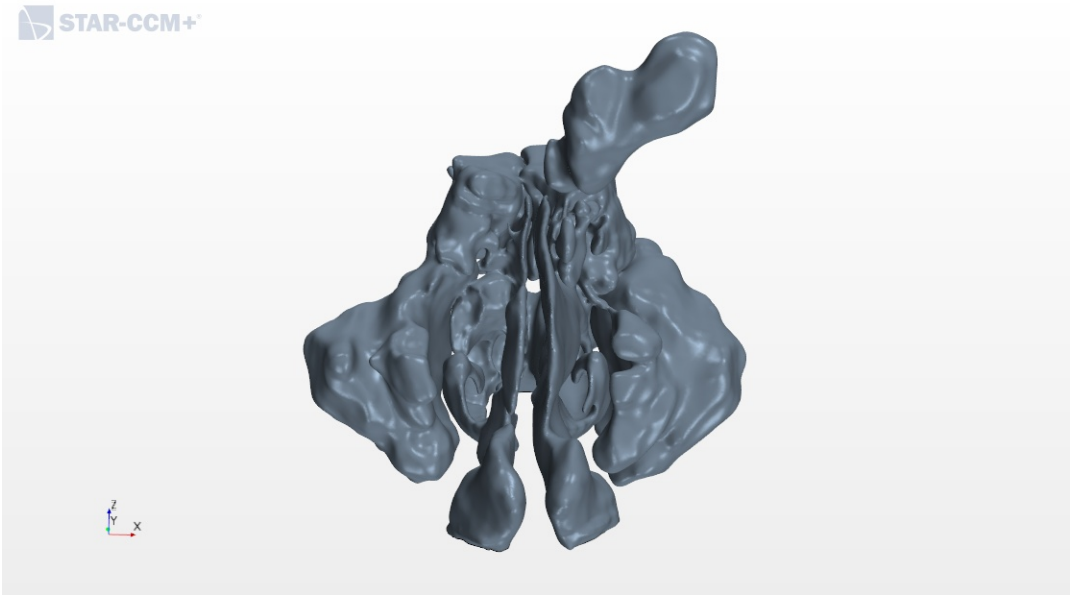

(b) Geometry 4.

Figure 6.2: Front view of the nasal channels.

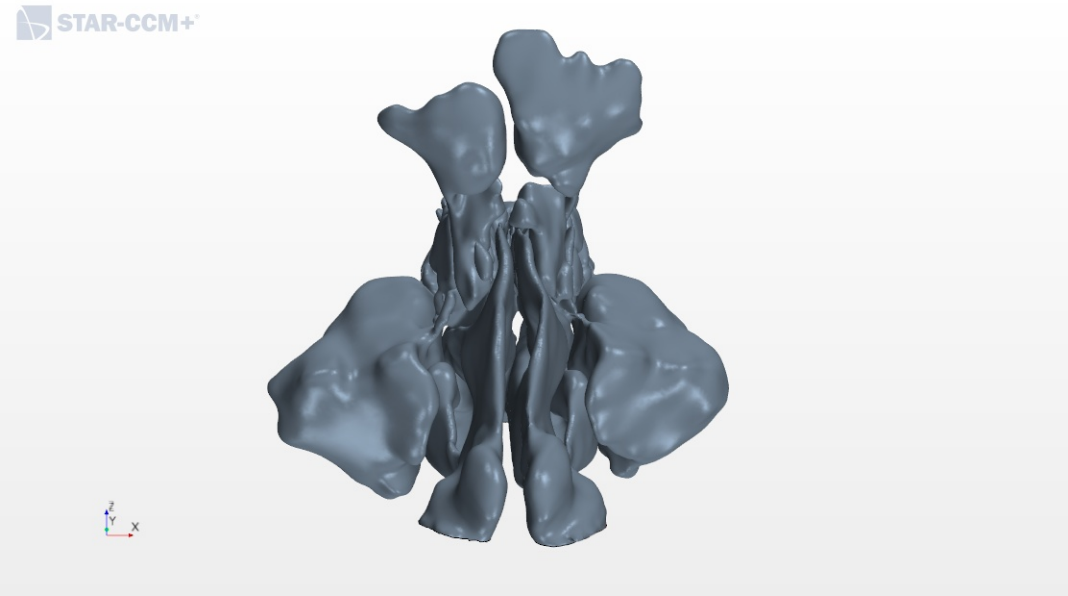

Figure 6.3: Front view of the nasal channels for geometry 5.

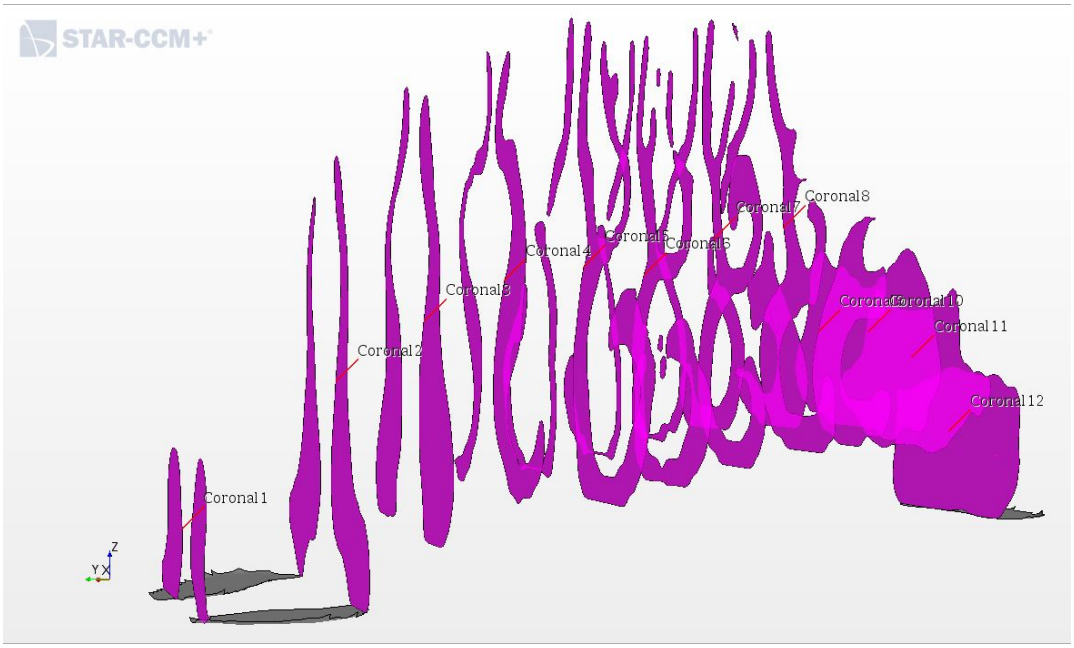

Figure 6.4: Locations of representative coronal cross sections in the CFD model. The nostrils are on the left and the nasopharynx on the right.

6.2 Preliminary analysis

Basic calculations had to be made before the simulations could be started to find necessary parameters for selection of boundary conditions. Thereby they are fundamental for realistic CFD simulation of the nasal passage.

The velocity magnitude in each model corresponds to a low rate of Q=166 ml/s based on Balakin et al. [2]. When simulating inhalation, the inlet velocity was estimated using the frontal area of both the nostrils, and the flow rate. The frontal area was computed by the software STAR-CCM+ from the CT-images. The calculated velocities were found to be between 1-2 m/s. Because of the low velocities, the flow was assumed to be incompressible due to a low Mach number (less than 0.3).

To determine the flow regime the Reynolds number had to be estimated. Both the inlet and outlet velocity at the nostrils and nasopharynx are used to indicate what flow regime to expect. Using the previously calculated velocities, as well as the geometry at the inlet, the Reynolds number of the flow was much lower than 2100. This indicates that the flow was laminar.

6.3 Mesh

Section 4.7 gives a describtion of the generation of computational mesh. In this thesis the surface remesher, prism layer mesher and polyhedral mesher were used. Below, their description is shown [31]:

- **Surface Remesher:** Used to improve the overall quality of an existing surface and optimize it for the volume mesh models. This remesher is also used to improve the surface for the volume meshers.
- **Prism Layer Mesher:** The prism layer mesh model is used with a core volume mesh to generate orthogonal prismatic cells next to wall surfaces or boundaries. This layer of cells is necessary to improve the accuracy of the flow solution.
- **Polyhedral Mesher:** This model provides a balanced solution for complex mesh generation problems, and is relatively easy and efficient to build.

The base size was set to 0.001 m for all the models, and the number of prism layers was equal to two. The size of the grid cells was adjusted to get a satisfactory result, however smaller cells require a longer computational time. This size of the grid was testet during Balakin et al. [2] mesh independence study and presented very satisfactory results. Figures 6.5 and 6.6 show the applied mesh.

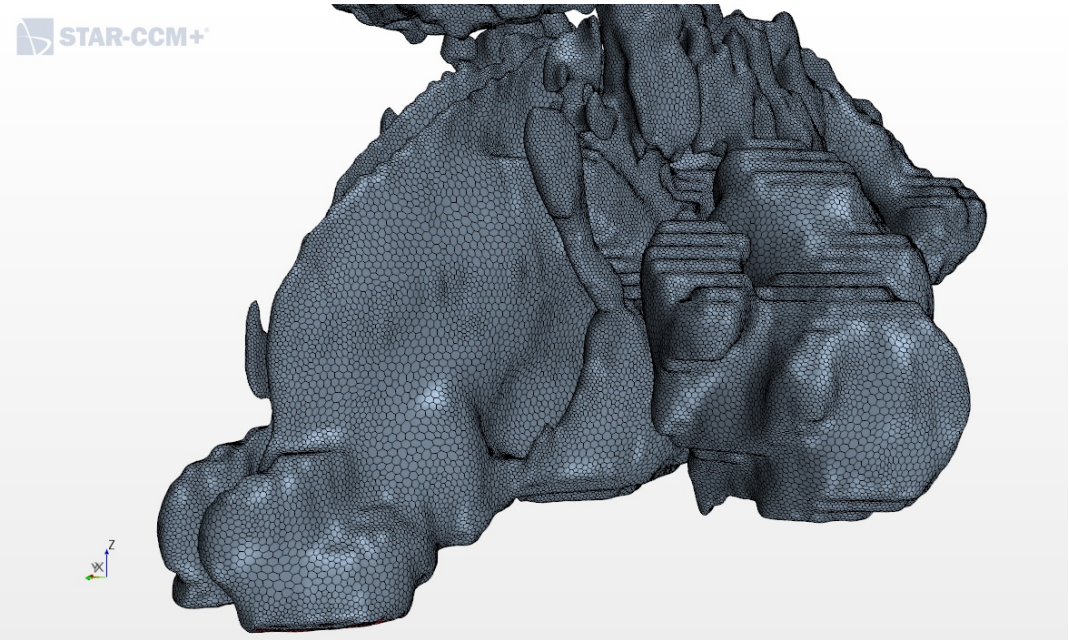

Figure 6.5: The volume mesh design, showing the form of the polyhedral mesh.

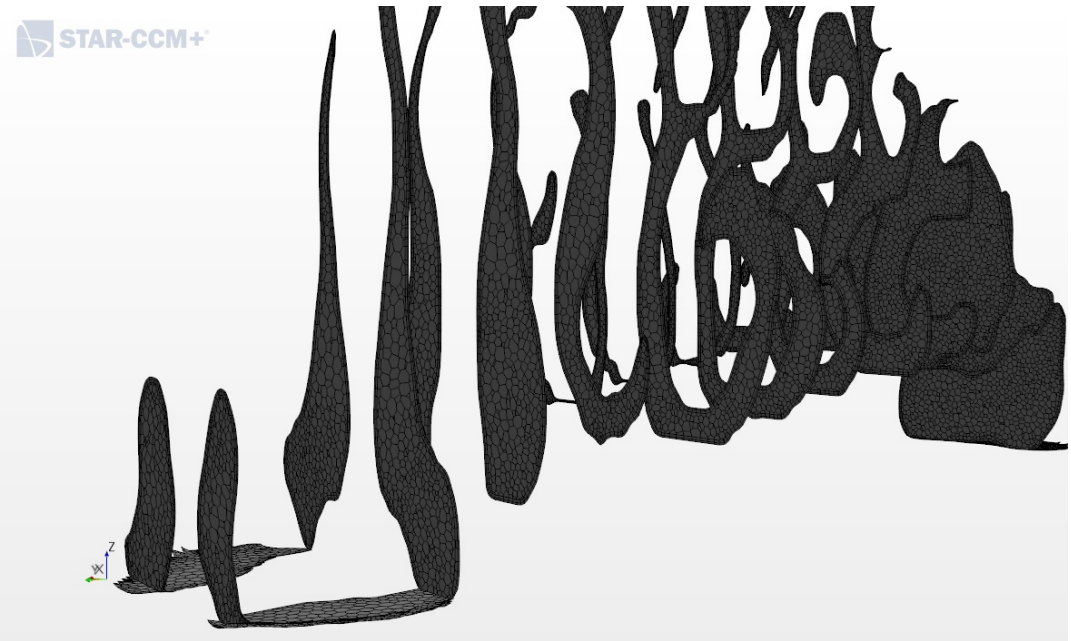

Figure 6.6: Polyhedral mesh applied on the 12 coronals.

6.4 Simulations

In this thesis several numerical simulations were run, fifteen in total. The details of the simulations are shown in Table 6.1.

Table 6.1: Overview over simulations that were conducted.

Model	Simulation	Measured parameters	Breathing
Geometry 1: Obstruction	1	Velocity, pressure and humidity	Inhalation
	2	Particle deposition	Inhalation
	3	Velocity, pressure and humidity	Exhalation
Geometry 2: ENS	4	Velocity, pressure and humidity	Inhalation
	5	Particle deposition	Inhalation
	6	Velocity, pressure and humidity	Exhalation
Geometry 3: ENS	7	Velocity, pressure and humidity	Inhalation
	8	Particle deposition	Inhalation
	9	Velocity, pressure and humidity	Exhalation
Geometry 4: Obstruction	10	Velocity, pressure and humidity	Inhalation
	11	Particle deposition	Inhalation
	12	Velocity, pressure and humidity	Exhalation
Geometry 5: Healthy	13	Velocity, pressure and humidity	Inhalation
	14	Particle deposition	Inhalation
	15	Velocity, pressure and humidity	Exhalation

6.5 Applied set of STAR-CCM+ models and solvers

Through the selection of physics models, the primary variables of the simulation and the mathematical formulation are used to generate a solution. The model main purpose is to work with solvers, which the solution is controlled by being activated once per iteration. Based on the description in the STAR-CCM+ user manual, a brief description of the physics models and solvers used in this thesis is presented in the following section [31].

This subsection is divided in two, since fluid flow uses other physics models than the particle deposition.

6.5.1 Velocity, pressure and humidity

The multi-component gas model defines the equation of state for the density of the gaseous phase, meaning air and water vapour in this thesis. As mentioned in Section 4.1 the density of the gaseous phase is assumed to be invariant throughout the continuum, meaning it will not vary with temperature and the reference pressure will not have any impact on the calculations when the constant density model is activated.

The flow specification for these simulations is segregated. The segregated flow model is used for incompressible or mildy compressible flows, especially when computational resources are an issue. The model activates the segregated solver, which is used to compute unknown variables: an equation for a certain variable is solved for all cells, then the equation for the next variable is solved for all cells, and so on [35]. The segregated species model solves the species continuity equations for a multi-component fluid mixture. Since the fluid in this thesis is a mixture of two gas components, the segregated species model solves two transport equations sequentially. The segregated species solver controls the solution update for the segregated species model.

This thesis investigates a laminar flow in a nasal cavity. In this regime, the fluid flow can be completely predicted by solving the Navier-stokes equations. The steady model used is a time model, and the primary function is to provide solvers that control the iteration, and it is used for all steady-state calculations. The gradient model is a function of position in the stream and therefore defines a field. The gravity model accounts for the action of gravitational acceleration in STAR-CCM+.

The cell quality remediation model helps to identify poor-quality cells by using a set of predefined criteria, and thereby contributes to solve poor-quality mesh. Once these cells and their neighbors have been marked, the computed gradients in these cells are modified in a way as to improve the strength of the solution.

6.5.2 Particle deposition

There are some models that are used in the particle deposition simulations, that are the same as mentioned in Subsection 6.5.1. They are: the cell quality remediation, constant density, gradients, laminar, gravity and multi-component gas. In the fol-

lowing other additional models are mentioned.

The flow specification in the simulation of particle deposition is coupled. The coupled flow model solves the conservation equations for mass, momentum and energy simultaneously using a pseudo-time-marching approach. Since the governing equations are non-linear and coupled, several iterations of the solution loop must be performed before a converged solution is obtained. The coupled species model is an extension of the coupled flow model, and is activated when a multi-component gas is chosen. With the coupled flow model, implicit unsteady approach is one alternative time model. In the approach, each physical time-step involves some number of inner iterations to converge the solution for that given instant of time.

The material particles model was chosen, which represents real particles of a physical substance, such as aqueous aerosols. Material particles have mass and volume, and the physical conservation laws of continuity and momentum govern their behavior. The particles are assumed to be internally homogenous and without internal motion. In the Lagrangian approach, models for the drag, shear lift, gradient pressure and virtual mass forces are applied. The corresponding equations and descriptions are mentioned in Section 5.2.

The coupled implicit solver controls the solution update for the coupled flow model. With the coupled solver, the conservation equations for continuity, momentum, energy, and species are solved simultaneously as a vector of equations. The implicit unsteady solver basic function is to control the update at each physical time for the calculation and the time-step size. The Lagrangian multiphase solver controls the update for the Lagrangian multiphase model. Depending on the selections in the physics continuum or Lagrangian phase, sub-solvers are added in the Lagrangian multiphase solver.

6.6 Additional essential parameters

The maximum inner iterations are a stopping criterion based on the number of inner iterations that the solver executes for transient analysis (means analyzing a system in unsteady state). The number of maximum inner iterations was set to two iterations per-one-time step.

The maximum physical time stopping criterion is based on the simulation time that has elapsed in a transient analysis, and the time was not set to a specified value during particle deposition, since the deposition time varied in each model.

Many multiphase flow simulations are naturally unsteady, and therefore it is difficult to reach convergence. Under-relaxation factors affect the convergence of numerical simulations, and are applied in numerical computing to stabilize the solution and reach the convergence faster. During all the simulations the default URFs values were used.

6.7 Injector

To introduce the particles of the dispersed Lagrangian phase, an injector was set up. The injector defines the initial state of the particles. There are several injector types in the simulation software, each with its own distinctive features that determine where and how the particles are injected. In this thesis the part injector was implemented. A part injector represents a collection of injection points that are extracted from the geometry of the parts of the injector. The nostrils (inlet 1 and 2) was the chosen parts in all five models. In this research, the particles mimic aqueous aerosols. In Table 6.2 the chosen conditions and values for the particle phase is shown. The particle velocity in each simulation was the same as the velocity inlet given in Table 6.7.

Table 6.2: The conditions and values chosen in the injector.

	Method/value
Flow rate distribution	Per injector
Flow rate specification	Particle flow rate
Particle size specification	Particle size
Parcel streams	1.0 (default value)
Particle diameter	$1.0 \cdot 10^{-5}$m (constant)
Particle flow rate	10000.0 /s (constant)

One subcategory in the Lagrangian phase injector model is the point inclusion probability (PIP) property, it sets the probability of a point being included in the set of points from which the particles are injected. The default value of PIP is 1.0, which means that the injector uses all points that are extracted from the part. In this study the value was adjusted: by lowering the value only a subset of the points was used [31]. By adjusting the PIP value, the quantity of particles injected could be modified. The objective was to inject about the same number of particles into the nostrils. However, all the models have different number of points in the nostrils, so that the PIP value and the corresponding number of particles differs slightly. See Table 6.3 for the selected PIP values and the number of particles injected into each model.

Table 6.3: Point inclusion probability values and the amount of particles injected.

Model	PIP value	Number of particles injected
Geometry 1: Obstruction	0.1	99
Geometry 2: ENS	0.1	89
Geometry 3: ENS	0.065	100
Geometry 4: Obstruction	0.1	95
Geometry 5: Healthy	0.095	96

6.8 Applied boundary conditions

Boundary conditions are applied to specify conditions on the domain boundary, to complete the mathematical models for the specific case. Boundary conditions are used on the faces that coincide with the boundaries of the computational domain [31]. The values that are not mentioned in this section were assigned default setting values.

A no-slip condition was set at the airway walls, meaning the air velocity was set to zero at the surface of the nasal membranes, which lines the nasal cavity. For particle deposition the Lagrangian phase boundary conditions on the wall was set to stick, thus the particles deposit on the wall when they touch the membrane. The molecular properties of the air-vapour mixture were found via mass-homogenization [2]:

$$\mu = \mu_{H_2O} c_{H_2O} + \mu_{air}(1 - c_{H_2O}), \tag{6.1}$$

$$\rho = \rho_{H_2O} c_{H_2O} + \rho_{air}(1 - c_{H_2O}), \tag{6.2}$$

$$k = k_{H_2O} c_{H_2O} + k_{air}(1 - c_{H_2O}), \tag{6.3}$$

and

$$c_p = c_{p,H_2O} c_{H_2O} + c_{p,air}(1 - c_{H_2O}). \tag{6.4}$$

The reference values of individual components are shown in Table 6.4.

Table 6.4: Molecular properties of the flow components.

	Air	Vapour (H_2O)
Density [kg/m^3]	1.184	0.595
Viscosity [Pa $\cdot$ s]	$1.855 \cdot 10^{-5}$	$1.268 \cdot 10^{-5}$
Thermal conductivity [W/m $\cdot$ K]	0.026	0.025
Specific heat [J/kg $\cdot$ K]	1004	1938

The mass fractions for the chosen species are listed in Tables 6.5 and 6.6, they are divided in two on the basis of whether inhalation or exhalation were simulated. The flow is always conditioned to 100 % relative humidity at the nasopharynx, also since the respiratory epithelium: thin tissue that cover all the exposed surfaces [36], is coated with mucosa, air was therefore assumed to be at 100 % relative humidity at the wall. At inhalation the climate conditions for relative humidity were set at 70 %. Tables 6.7 and 6.8 show the parameters set at the boundaries.

Table 6.5: Species mass fraction and temperature at inhalation.

Part	Air	Vapour (H_2O)	Temperature
Inlet 1 and 2 (nostrils)	0.987631	0.012369	300 K
Outlet (nasopharynx)	0.96306	0.03694	305.6 K
Wall	0.96306	0.03694	305.6 K

Table 6.6: Species mass fraction at exhalation.

Part	Air	Vapour (H_2O)	Temperature
Inlet (nasopharynx)	0.96306	0.03694	305.6 K
Outlet 1 and 2 (nostrils)	0.987631	0.012369	300 K
Wall	0.96306	0.03694	305.6 K

Table 6.7: Boundary conditions for all the models at inhalation. Inlet is the nostrils and outlet at the nasopharynx.

Model	Part	Boundary conditions	Magnitude (in z-direction)
Geometry 1: Obstruction	Inlet	Velocity inlet	1.145 m/s
	Outlet	Pressure outlet	0 Pa
Geometry 2: ENS	Inlet	Velocity inlet	0.984 m/s
	Outlet	Pressure outlet	0 Pa
Geometry 3: ENS	Inlet	Velocity inlet	0.952 m/s
	Outlet	Pressure outlet	0 Pa
Geometry 4: Obstruction	Inlet	Velocity inlet	1.615 m/s
	Outlet	Pressure outlet	0 Pa
Geometry 5: Healthy	Inlet	Velocity inlet	1.02 m/s
	Outlet	Pressure outlet	0 Pa

Table 6.8: Boundary conditions for all the models at exhalation. Inlet is the nasopharynx and outlet at the nostrils.

Model	Part	Boundary conditions	Magnitude (in z-direction)
Geometry 1: Obstruction	Inlet	Velocity inlet	1.29272 m/s
	Outlet	Pressure outlet	0 Pa
Geometry 2: ENS	Inlet	Velocity inlet	1.0818 m/s
	Outlet	Pressure outlet	0 Pa
Geometry 3: ENS	Inlet	Velocity inlet	0.9 m/s
	Outlet	Pressure outlet	0 Pa
Geometry 4: Obstruction	Inlet	Velocity inlet	1.0684 m/s
	Outlet	Pressure outlet	0 Pa
Geometry 5: Healthy	Inlet	Velocity inlet	1.624 m/s
	Outlet	Pressure outlet	0 Pa

Chapter 7

Results and discussion

This chapter shows the results from all the simulations listed in Table 6.1. They are presented in series of snapshots, plots and tables. Further, this chapter discusses the results.

7.1 Pressure and resistance

The intra-nasal pressure is an important parameter, related directly to the breathing function [2]. The pressure measurements were conducted in 10 different simulations. Figures 7.1 and 7.2 show the pressure distribution during inhalation and exhalation, respectively. The pressure is plotted in the 12 coronal cross-sections. Coronal 1 is nearest the nostrils, and coronal 12 is at the nasopharynx. Additionally, in Appendix B there are snapshots of the pressure distribution in the nasal cavity. Furthermore, in Appendix B there are plots showing how the pressure is distributed in respectively the right and left nasal cavity.

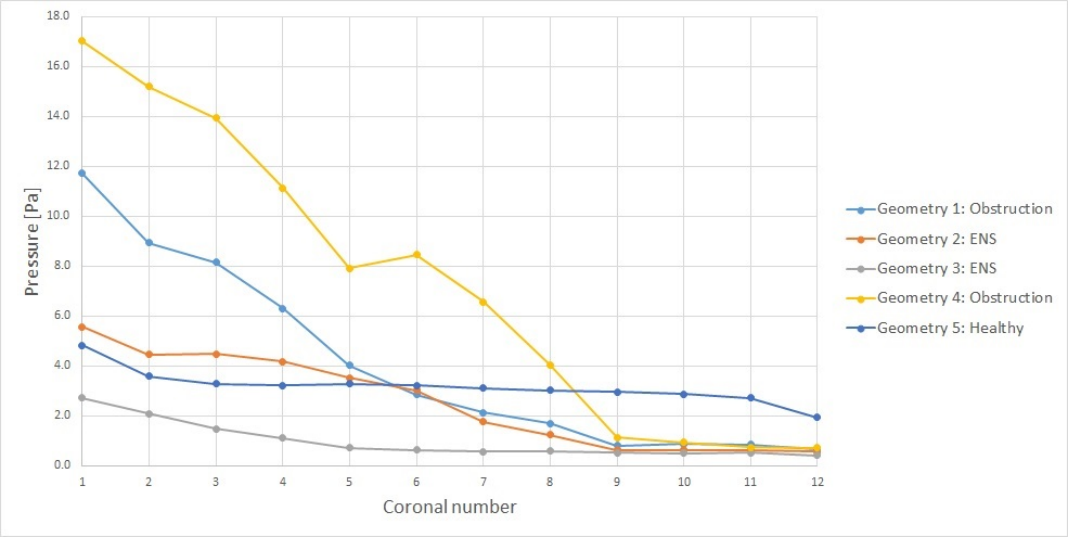

Figure 7.1: Pressure distribution in the nasal cavity at inhalation.

During inhalation, the highest pressure for the airflow is recorded at the anterior part of the nose: at the head of the inferior and the middle turbinate in the nasal valve (the first quarter of the coronal). This is shown in Figure 7.1. The pressure decreases as the distance from the anterior nose increases. The two models with ENS show a rather modest reduction near the nasal valve compared to the cases with obstruction. This is the same as found in Balakin et al. [2], and can be explained by the difference

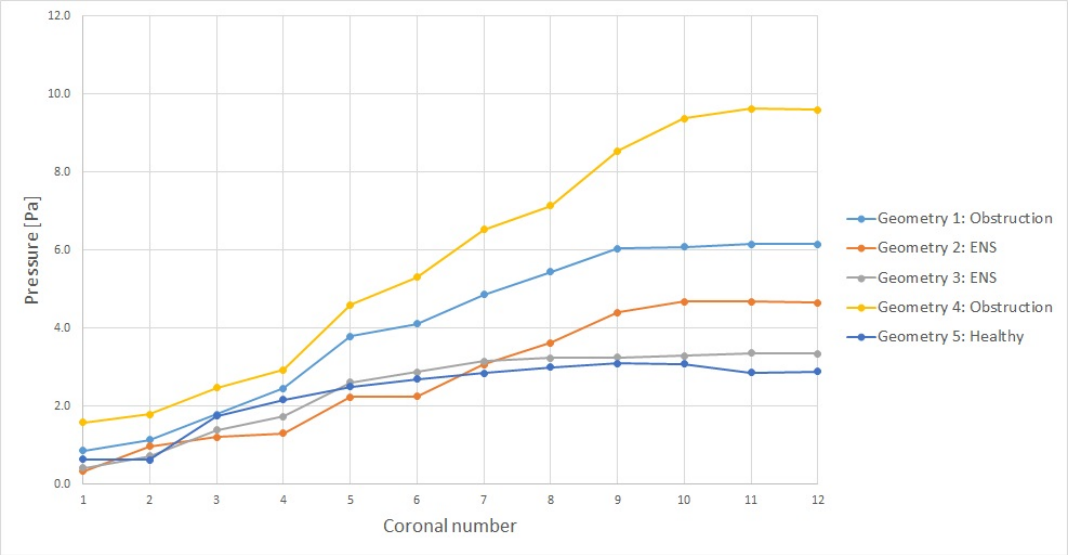

Figure 7.2: Pressure distribution in the nasal cavity at exhalation.

caused by the partial operational expansion of the channels in the ENS geometries. This results in a relatively similar pressure reduction toward the nasopharynx as in the model for the case of the healthy patient.

During exhalation, the fluid is expelled from the lungs. There is therefore a predominance of higher values of pressure during exhalation at the posterior of the nasal cavity. By comparison, for the healthy- and ENS models the pressure during inhalation at coronal 1, is relatively similar to the pressure found at coronal 12 in the exhalation phase, see Figure 7.2. On the other hand, for geometry 1 and 4 with an obstruction in the nasal cavity we observe lower pressure at the start of the exhalation phase than the inhalation phase. Figure B.1 and B.7 see Appendix B representing geometry 1 and 4, respectively, show that the right nasal cavity in both models at inhalation has a considerable higher pressure than the left cavity. This can be explained by the low CSA found in the right nasal cavity, displayed in Figures A.2 and A.5.

The nasal airway resistance is the resistance of the respiratory tract to airflow, at inhalation and exhalation. It is an important factor when considering the total nasal airway resistance, because nasal breathing is responsible for around 50 % to 80 % of all airway-resistance. This resistance results from the friction between streaming air and mucosa [14]. In addition, the resistance plays a vital role in preventing collapse of lung [37]. The formula used to calculate the resistance is [20]:

$$R = \frac{\Delta P}{Q}, \tag{7.1}$$

where R is the nasal resistance of the cavity, ΔP is difference of pressure between the nostrils and nasopharynx, and Q is the volumetric flow rate through the nasal cavity. The calculated values are shown in Tables 7.1 and 7.2.

Table 7.1: Flow resistance of the models at flow rates of 166 ml/s at inhalation.

Model	Flow resistance $[\frac{\text{Pa·s}}{\text{ml}}]$
Geometry 1: Obstruction	0.06131
Geometry 2: ENS	0.03397
Geometry 3: ENS	0.01728
Geometry 4: Obstruction	0.09682
Geometry 5: Healthy	0.01617

Table 7.2: Flow resistance of the models at flow rates of 166 ml/s at exhalation.

Model	Flow resistance $[\frac{\text{Pa·s}}{\text{ml}}]$
Geometry 1: Obstruction	0.03037
Geometry 2: ENS	0.02458
Geometry 3: ENS	0.01587
Geometry 4: Obstruction	0.03745
Geometry 5: Healthy	0.03213

Based on the calculations a lower resistance is found at exhalation for all the models except for the case of the healthy patient. The largest difference in resistance is seen in the two obstruction models which correlates with the pressure results seen in Figures 7.1 and 7.2. This is as mentioned earlier most likely due to the lower open area in the nasal cavity compared to the other geometries. The nasal valve during inhalation contributes to the maximum of the nasal airway resistance, since the dimension of this area is governed by the size of the IT and the nasal septum. Swelling of this structure has an important determining effect on the nasal resistance. Airway resistance is also determined by the balance between the forces tending to narrow the airways and the forces tending to widen them [38]. Reduction of the airway diameter drastically increases its resistance, whereas dilation of the airway can significantly reduce its resistance [39]. ENS patients have undergone some form of surgical enlargement of the internal nasal channels, thus, may be the reason for the very low resistance seen for geometry 3 in Figure 7.1. This were pointed out by Sceithauer [14], where he said that by expansion of the nasal cross-section, respiratory resistance is reduced and thus the pressure gradient at the interface of air and mucosa. Reduced aerodynamic resistance induced by channel modification may alter nasal aerodynamics. The potential outcome could be sensitive changes in microclimate and sensation and thereby alter the pulmonary function [2].

Riazuddin et al. [21] obtained lower resistance values during exhalation than at inhalation. The same did Haight et al. [40] find during quiet respiration. However, Kenyon [41] noted the opposite, that is, the exhalation resistance being higher than

the inhalation resistance. Further, Viani et al. [42] observed during low flow rates a higher resistance during exhalation flow than during the inhalation flow. All the subjects in the studies were healthy with no persistent nasal symptoms. Viani and Kenyon results correlate to the healthy patient in the present research. At exhalation there is a lower difference in pressure and nasal resistance values between all the models than at inhalation. Haight et al. In Zu et al. [20] a higher nasal resistance for the deviated noses was observed, than in the undeviated case. The same was observed in this thesis, where the obstruction models lead to a higher nasal resistance. Thus, the influence of geometrical variations are found to produce significant differences in the resistance.

7.2 Streamlines

Nasal airflow is essential for an adequate intranasal climate, and it is not only driven by the path of least resistance, but also by its momentum [18, 22]. Streamlines are released from the inlets, and are used to visualize the flow path inside the nasal cavity. Snapshots from three models are presented in this section, and the remaining ones can be seen in Appendix D. The figures are divided into four subframes where one frame shows streamlines from the right nostril, and another frame displays streamlines from the left nostril at inhalation. The two remaining frames show streamlines from the nasopharynx to either the right or left nostril at exhalation. All subframes are shown in Figure 7.3. This is done in order to visualize the path of the streamlines more clearly, since there is a difference in how the streamlines are distributed in the left and right nasal cavity. In addition, an overview of how the nasal cavity is divided into three regions is shown in Appendix C, to give a better illustration of the process.

For the case of the healty patient, see Figure 7.3, the flow had similar uniform distribution during both inhalation and exhalation, and the streamlines did not show any kind of preferred path. However, a difference in the airflow streamlines pattern is observed in the two ENS geometry models. For geometry 3 the streamlines show a more uniform distribution of airflow in the nasal cavity at exhalation than at inhalation, which can be seen in Figures 7.4 and 7.5. In the right nasal cavity of geometry 3, majority of the airflow is observed in the inferior region at inhalation, in comparison to the left nasal cavity where the streamline patterns for the most part is observed in the MT region, shown in Figures 7.4a and 7.4b. At exhalation a more evenly distribution of airflow pattern is seen, see Figures 7.4c and 7.4d. The same streamlines pattern at inhalation and exhalation are seen in the left nasal cavity for geometry 2.

Li et al. [22] studied the streamlines in the nasal cavity for ENS patients at inhalation. The computed streamlines in the present research were in general agreement with those found by Li et al. Their study showed that during inhalation the airflow pattern in the nasal cavity to the ENS geometries left majority of the IT region without air movement (Figure 3.1). The airflow was concentrated in the middle meatus region, this is observed in Figure 7.4b, likewise in Figure 7.5b in the posterior region of the nasal cavity. The nasal airflow has a natural tendency of moving

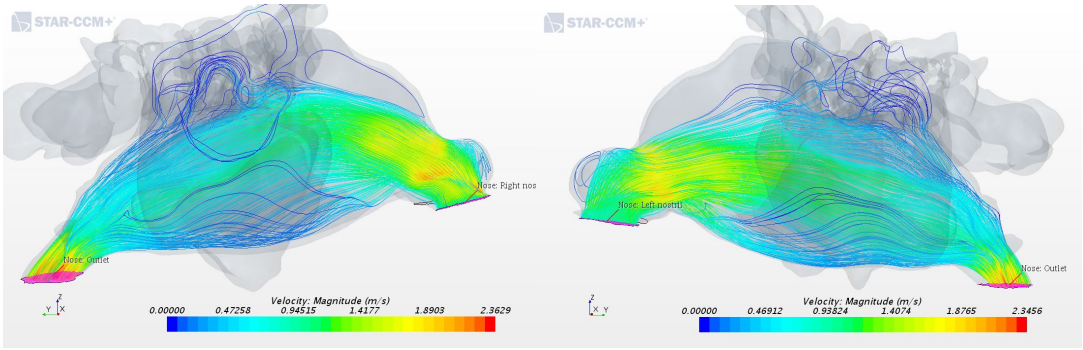

(a) Inhalation: streamlines from the right nostril.

(b) Inhalation: streamlines from the left nostril.

(c) Exhalation: streamlines from the nasopharynx and out the right nostril.

(d) Exhalation: streamlines from the nasopharynx and out the left nostril.

Figure 7.3: Airflow patterns for geometry 5, displayed by streamlines during inhalation and exhalation.

upwards through the middle meatus region if the proper structures are not in place to distribute the airflow. This is caused by the fact that the airflow must turn 180 degrees to flow into the lungs in the downward direction, after entering the nostrils in the upright direction. As observed at the posterior part of the nasal cavity during exhalation in Li et al. and in this thesis, there is a high velocity close to the upper roof of the nasal cavity. This is due to the anatomical features of the nasopharynx that throws the air to the top.

As seen from the results, for the case of the healthy patient has a more uniform distributed airflow in the nasal cavity, which theoretically improves efficiency. Healthy nasal turbinates play a critical role in partitioning the nasal airflow, and better facilitate the normal nasal physiology. This results in a better capability to warm, humidify, and filter the inhaled airflow, while preventing unwanted dehydration of the mucosa [22]. A symptom that most ENS patients experience is dryness in the nasal cavity, and the parted airflow may contribute to this phenomenon.

Re-circulatory flow known as vortices, was prominently observed during exhalation in Riazuddin et al. [21]. The re-circulatory flow was detected at the floor of the posterior region. In the present study, vortices were also observed, but for the most part in the exhalation phase. The vortical-like structures ensure the air to linger within

the nose for a longer period. This results in enhancing the moistening of the inhaled air, as well as the senses of smell and taste that lie above the upper turbinate in the olfactory region [43]. Zu et al. [44] concluded that formation of swirls at the anterior heads during inhalation might be due to the abrupt change of the nasal morphology. In this case, there are no well-defined vortices for the most part at the anterior part of the nasal cavity, and near the olfactory-region during inhalation. One reason may be the low inlet velocity and the volumetric flow rate. McCabe et al. [45] pointed out that vortices are most frequently encountered when there is an abrupt change in the flow channel, such as a sudden expansion or contraction, a sharp bend, or an obstruction around which the fluid mostly flows. By removing the structures in the nose, and thus opening the nasal cavity, for example by severe turbinate reduction, the less vortices can occur, thus contributing to making a poorer environment in the nasal cavity.

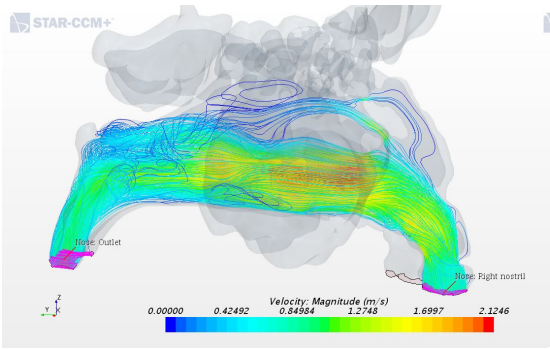

(a) Inhalation: streamlines from the right nostril.

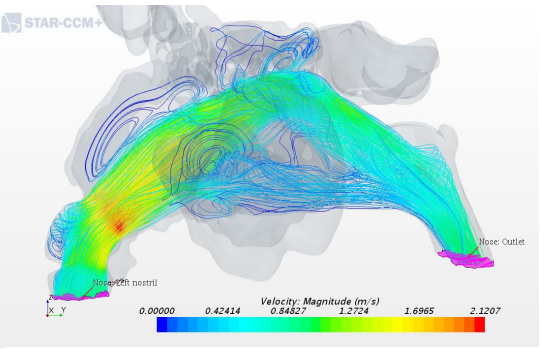

(b) Inhalation: streamlines from the left nostril.

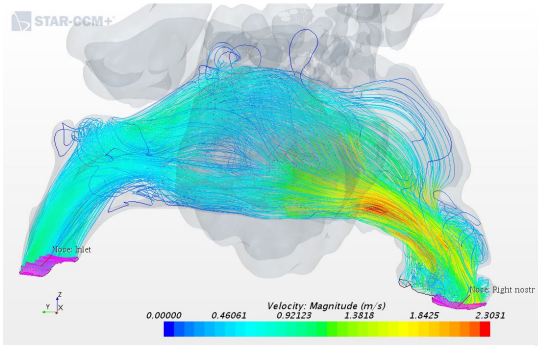

(c) Exhalation: streamlines from the nasopharynx and out the right nostril.

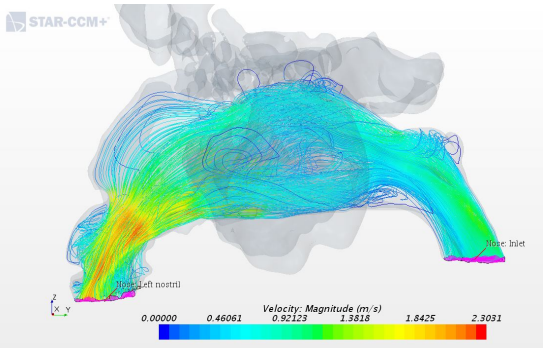

(d) Exhalation: streamlines from the nasopharynx and out the left nostril.

Figure 7.4: Airflow patterns for geometry 3, displayed by streamlines during inhalation and exhalation.

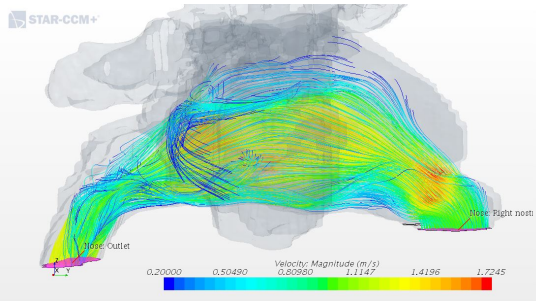

(a) Inhalation: streamlines from the right nostril.

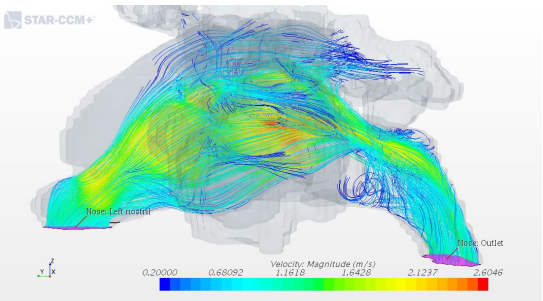

(b) Inhalation: streamlines from the left nostril.

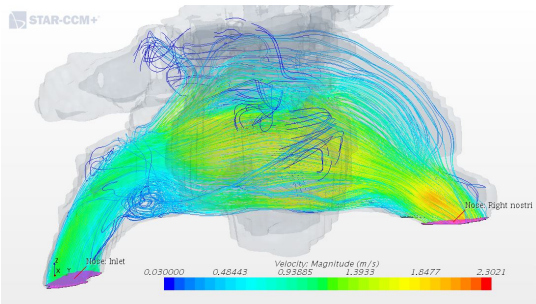

(c) Exhalation: streamlines from the nasopharynx and out the right nostril.

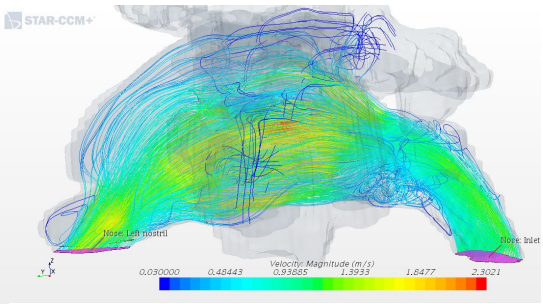

(d) Exhalation: streamlines from the nasopharynx and out the left nostril.

Figure 7.5: Airflow patterns for geometry 2, displayed by streamlines during inhalation and exhalation.

7.3 Flow partitioning in the nostrils

Flow partitioning is defined as the proportion of air flowing through the left and right airway. In this case the flow partitioning in the nostrils were calculated to see if the distribution changed in the left and right nostril at inhalation and exhalation. The volumetric flow rate, Q in the nostrils was calculated based on the frontal area of each nostril, and the velocity at the respective inlets. The results of the calculations of the flow partitioning in each nostril is presented in percent and shown in Tables 7.3 and 7.4. Also snapshots of two models showing the velocity distribution in the nostrils are shown in this section, the remaining ones are presented in Appendix E.

Table 7.3: Flow partitioning in the nostrils (%) at inhalation (Geom. = Geometry).

	Geom. 1: Obstruction	Geom. 2: ENS	Geom. 3: ENS	Geom. 4: Obstruction	Geom. 5: Healthy
Right (inlet 1)	52.72 %	48.83 %	50.98 %	46.88 %	49.71 %
Left (inlet 2)	47.27 %	51.17 %	49.02 %	53.12 %	50.39 %

In all five models, the estimated results show a change in which nostril has the highest distributed volumetric airflow from inhalation to exhalation. The most excessive difference is seen at exhalation and in the two geometries with an obstruction in the

Table 7.4: Flow partitioning in the nostrils (%) at exhalation (Geom. = Geometry).

	Geom. 1: Obstruction	Geom. 2: ENS	Geom. 3: ENS	Geom. 4: Obstruction	Geom. 5: Healthy
Right (outlet 1)	26.56 %	59.69 %	48.15 %	22.36 %	51.88 %
Left (outlet 2)	73.55 %	40.31 %	51.85 %	77.64 %	48.12 %

nasal cavity. The flow partitioning for geometry 1, shifted between the two nostrils from 52.72 % right and 47.27 % left to 26.56 % right and 73.55 % left. The same large difference was seen for geometry 4, the reason are the structures in the nasal cavity that prevent the air to flow easily through the nasal cavity during exhalation.

In the case of Hildebrandt et al. [19], the overall flow partitioning between two nasal cavities, one a healthy and the other a symptomatic case were analyzed. The flow partitioning in the two nasal cavities shifted from 56 % right and 44 % left to 53 % right and 47 % left. This was because of a decline in the flow space constriction in the anterior part of the left nasal cavity, which was a result of a repaired deviated septum. A similar shift can also be seen in geometry 1, where a comparison could be made based on pre-and post-operation geometries. The result shows a shift in the flow partitioning rate distribution from 26.56 % right and 73.55 % left at exhalation for geometry 1 to after operation 59.69 % right and 40.31 % left for geometry 2. The velocity distribution is visually illustrated in Figures 7.6 and 7.7, where the nostril with the highest velocity also is the one with the highest flow partitioning percentage out of the two nostrils.

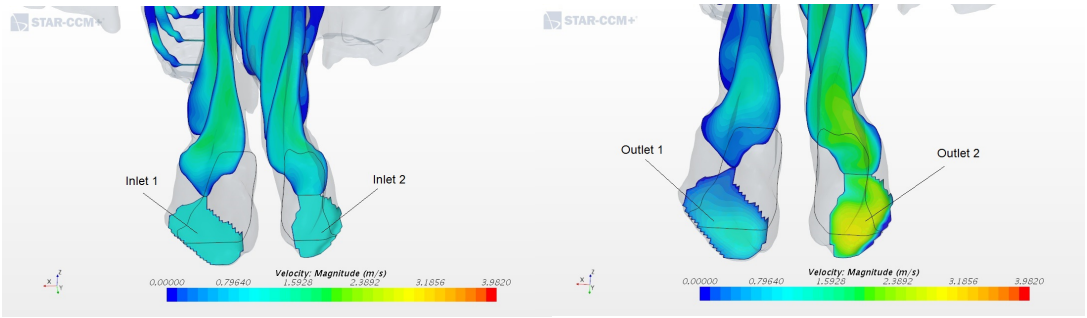

(a) Inhalation. **(b)** Exhalation.

Figure 7.6: Velocity distribution in the nostrils for geometry 1.

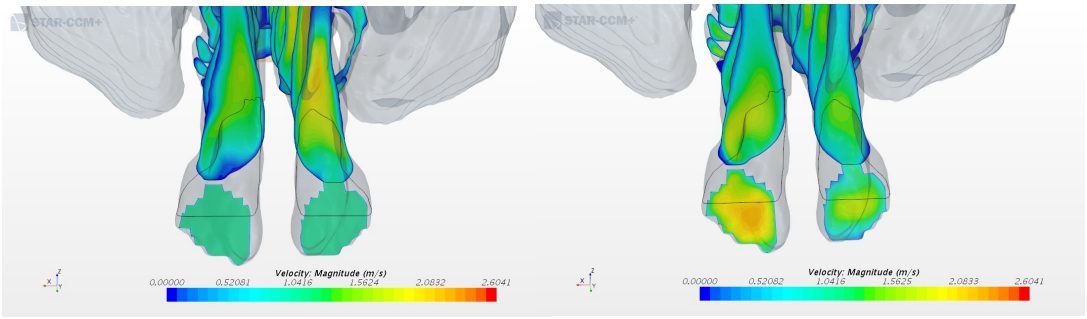

(a) Inhalation. **(b)** Exhalation.

Figure 7.7: Velocity distribution in the nostrils for geometry 2.

7.4 Humidity

Humidity is an important parameter for ENS patients, because it is associated with the sensation of the nasal patency. As mentioned earlier, among ENS patients a sensation of a blocked nose despite nasal patency is common. One factor that influences the sensations is the adequate mucosal cooling. Variables that affect mucosal cooling include nasal surface area and airflow characteristics. Air must reach all mucosal surfaces in order for adequate warming and humidification of inhaled air and consequently effective mucosal cooling to occur. When the overall surface area of the nasal passage is reduced and the airflow pattern is altered, as is the case for ENS patients, mucosal cooling is compromised, and so the sensation of nasal patency is not elicited [46].

Studies have been made on inner nasal temperature and humidity for both healthy and ENS geometries during inhalation, where Balakin et al [2] is one of them. Therefore, in this research humidity and temperature were simulated during both inhalation and exhalation. One important physiologic factor that separates ENS patients and healthy patients is a drier and colder climate in the nasal cavity. It is an important physiological symptom because it further impairs the sensation of airflow. The objective was to analyze differences in humidity between the geometries at inhalation and exhalation.

A total of ten simulations were run with the flow always conditioned to 100 % relative humidity at the nasopharynx and the wall inside the nasal cavity. The results showed 100 % humidity throughout the nasal cavity during exhalation, reason for this was that the air was very humid with a homogeneous distribution. Thus in the further work, it is planned to simulate with different climates conditions during exhalation.

7.5 Particle deposition

The particles, which deposit in the nasal cavity during inhalation do not reach the lungs, the nose acts as a protective barrier against lung deposition, and as a target tissue for deposited materials. Nasal deposition is important in relation to estimation of toxic dose from inhaled aerosols [47]. Therefore, in this research simulations were conducted to see if the different intra nasal structures and conditions in the five models had any influence on the number of particles deposited.

Five simulations of particle deposition were completed and analyzed, the ratio of number of particles deposited divided by number of particles injected are shown in Table 7.5. Snapshots of the models with the particles deposited are shown in this section and the remaining ones can be found in Appendix F. The result show the highest ratio of 0.5789 for geometry 4. The deposition ratio for geometry 3 is 0.18 which is the lowest ratio obtained for all the models. Further, the particles deposited in the nasal cavity for geometry 3 can be seen in Figure 7.8. There are several factors, which may affect these ratios.

Table 7.5: Particle deposition in the nasal cavity.

Model	Number of particles injected	Number of particles deposited	Ratio
Geometry 1: Obstruction	99	51	0.5152
Geometry 2: ENS	89	41	0.4607
Geometry 3: ENS	100	18	0.1800
Geometry 4: Obstruction	95	55	0.5789
Geometry 5: Healthy	96	38	0.3958

Firstly, patients with ENS have undergone nasal surgery, for example septoplasty or turbinate reduction surgery. The nasal mucosa can be reduced during this kind of surgeries. Nasal mucosa is important for particle deposition, because the particles will stick to the moist surface of the nasal mucosa, and thus do not reach the lungs. Geometry 2 shows a lower deposition ratio compared to the pre-operative model of geometry 1. This is in spite of the fact that a lower CSA is observed between coronal number 5-9 for geometry 2 according to Figure A.1. Thus, the lower ratio of particles deposited may be due to lack of nasal mucosa, and the sensitive changes in microclimate seen in ENS patients. A high number of particles is seen in the nasal cavity of geometry 4, the reason is most likely the obstruction on the right side. Where the particles deposit. This can be seen in Figure 7.9. Cheng et al. [25] point out that a smaller cross-sectional area indicates a higher nasal deposition, which corresponds to the results shown in Table 7.5.

ENS patients usually have a wider passage of the nasal cavity, this causes the bulk of inhaled air to have little contact with the remaining mucosal wall. Sozansky et al. [46] point out that with a reduced mucosal surface area for the air to interact with, and a lack of physiologic turbulent airflow seen in ENS patients, the nasal mucosa cannot carry out its primary functions of air conditioning and cleaning of particles.

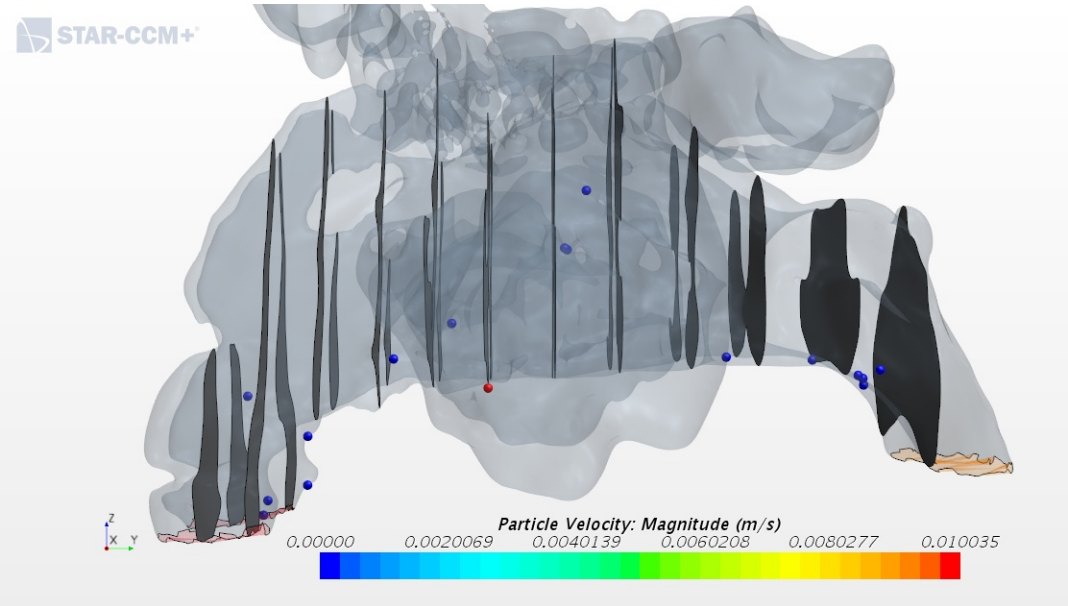

Figure 7.8: Lateral view of the particles deposited in the nasal cavity for geometry 3.

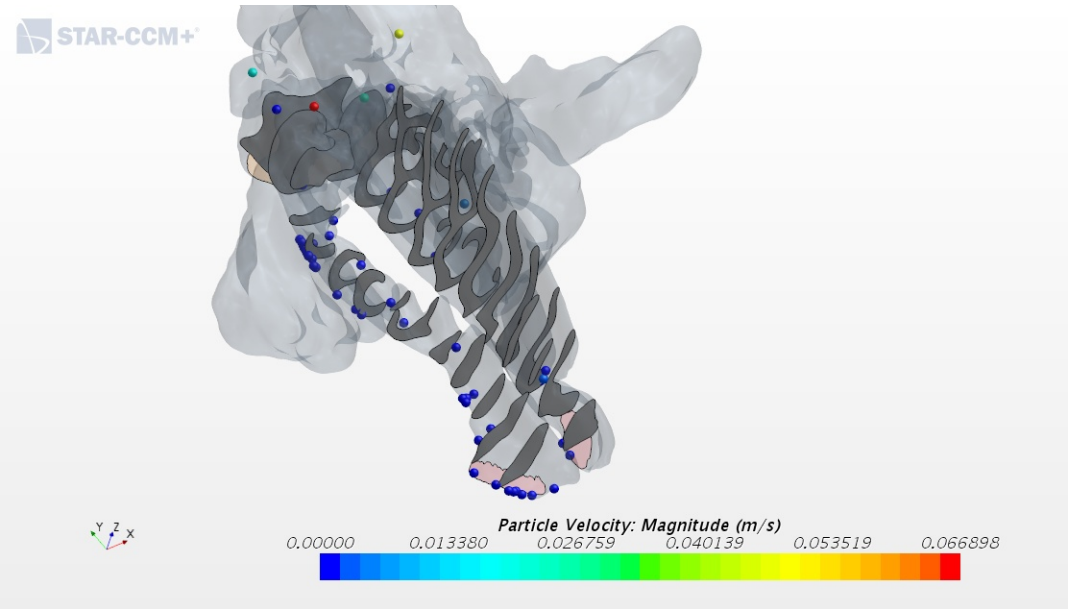

Figure 7.9: Snapshot taken from above of the particles deposited in the nasal cavity for geometry 4.

This could be connected to what was discussed in Section 7.2. The airflow in the ENS and obstruction geometries did not have the same uniform velocity distribution as for the case of the healthy patient. Keck et al. [18] explain how variations of airflow patterns entail varying contact times of the inhaled air to the surrounding mucosa, and that during turbulent airflow an increase in kinetic energy occurs and allows an intensified contact between inhaled air and mucosa. The slow airflow would

seem to be beneficial as it increases the time when air can be in contact with mucosa. However, the laminar quality of the slow airflow in ENS patients prevents extensive interaction of flowing air particles with the nasal mucosa [46]. Thus, in further research it is planned to simulate with a higher volumetric flow rate at the inlet.

Individuals with poor nasal filtration may be more susceptible to adverse health effects when exposed to airborne particulate matter, due to the resulting greater lung deposition. One of the results in Garcia et al. [48] study, showed poor nasal filtration in the atrophic rhinitis patient compared to the healthy subjects. Atrophic rhinitis is a chronic nasal condition, in which the patients have a progressive wasting away or decrease in size of the mucosa [49]. That may be transmissible in the way of mucosa reduction has an impact on particle deposition. Li et al. [22] mentioned in their study how turbinate surgery technique based on mucosal saving has now become the pillar to preserve mucosa and prevent complications, but also the need to find ways to preserve a healthy air-mucosal stimulation. Without the airflow stimulation, even healthy mucosal may not be sufficient to function properly.

Lastly, the geometry of the nasal cavity can be affected by the nasal cycle during breathing. This may affect the number of particles deposited. Baraniuk et al. [50] explained the nasal cycle as consisting of periodic congestion and decongestion of the nasal venous sinuses that leads to obstruction and patency, respectively, of each nostril. It is a physiologic phenomenon, which has been reported in more than 80 % of normal individuals, and is an important consideration when a patient undergoes a CT or MRI scan since the scan is an instant snapshot in time of the nasal cavity physiological state [8]. Cheng et al. [25] discussed how the nasal cycle could affect the number of particles deposited, and that the cross-sectional area may be affected by congestion of nasal passages due to infections and allergic reactions, and by subsequent decongestion from taking therapeutic drugs.

Considering the nasal cycle concept, mentioned in Section 7.3, only 22.36 % of the volumetric flow rate left out the right nostril for geometry 3. This percent may further reduce during the congestion phase.

Chapter 8

Concluding remarks and further work

This study aimed to present flow patterns in the nasal cavity, and compare nasal aerodynamics during inhalation and exhalation between geometries acquired by means of CT data from four individuals, where two have developed ENS, by using CFD software STAR-CCM+. In addition, inhaled particles deposition and clearance in the nasal cavity were studied.

Based on the results of this study, the influence of geometrical variations in the nasal cavity was found to produce quite large differences in the physical parameters when the cross-section was changed. This was seen in the pressure and resistance results for the obstruction models where an increase in resistance was seen because of the blockage on one side in the nasal cavity. Geometry 3 with ENS showed a very low resistance value at inhalation of 0.01728 Pa·s/ml and at exhalation 0.01587 Pa·s/ml compared to the other models, most likely due to the surgical enlargement that ENS patients have undergone. Furthermore, the overall resistance value was lower at the exhalation phase compared to the inhalation phase for all the models except for the healthy patient.

The humidity analysis showed a 100 % relative humidity throughout the nasal cavity during exhalation, reason for this was that the air was very humid with a homogeneous distribution. Therefore in the further work, it is planned to simulate with different climates conditions during exhalation.

The observed streamlines were relatively more uniformly distributed in the nasal cavity at exhalation than at inhalation for all the models. Furthermore, vortices were observed in the posterior region of the models at exhalation. Flow partitioning in the nostrils showed a change from which nostril had the highest volumetric flow rate from inhalation to exhalation. The largest difference was seen in the two obstruction models. For further work, simulation with a higher volumetric flow rate at the inlets will be a priority.

The highest particle deposition ratios were seen in the two models with an obstruction in the nasal cavity. ENS geometry 3 showed a particle deposition ratio of 0.18 that was much lower than for the other patients. Further, geometry 2 had a lower particle deposition ratio after the patient developed ENS, despite more patency in the nasal cavity. In this case the deposition ratio went down from 0.5152 to 0.4607. This may be due to the reduced mucosal area, which is common in ENS patients. However, to reveal if the reduced mucosa may influence the low deposit ratio, for fu-

ture work it would be preferable to use a larger sample of ENS patients. In addition, a larger number of CT-images from healthy patients would be required for comparison. Further, there is a need to have access to more sets of pre- and post-operation CT-images.

Bibliography

[1] "Empty Nose Syndrome: Treatment, Symptoms, and Death." [Online]. Available: https://www.healthline.com/health/empty-nose-syndrome. Accessed: 2018-01-18

[2] B. V. Balakin, E. Farbu, and P. Kosinski, "Aerodynamic evaluation of the empty nose syndrome by means of computational fluid dynamics," *Computer Methods in Biomechanics and Biomedical Engineering*, vol. 20, no. 14, pp. 1554–1561, Oct. 2017.

[3] "Empty Nose Syndrome." [Online]. Available: http://www.usasinus.org/empty-nose-syndrome/. Accessed: 2018-02-19

[4] "Nasal Mucosa." [Online]. Available: http://emptynosesyndrome.org/turbinate-tutorial/nasal-mucosa. Accessed: 2018-01-24

[5] "Empty Nose Syndrome Dr. Med. Robert Bodlaj." [Online]. Available: https://www.schlafmedizin-praxis.de/en/schwerpunkte/empty-nose-syndrome/. Accessed: 2018-03-27

[6] "Empty Nose Syndrome." [Online]. Available: http://ensassociation.org/. Accessed: 2018-02-05

[7] C. Li, A. A. Farag, J. Leach, B. Deshpande, A. Jacobowitz, K. Kim, B. A. Otto, and K. Zhao, "Computational fluid dynamics and trigeminal sensory examinations of empty nose syndrome patients," *The Laryngoscope*, vol. 127, no. 6, pp. E176–E184, Jun. 2017.

[8] J. Tu, K. Inthavong, and G. Ahmadi, *Computational Fluid and Particle Dynamics in the Human Respiratory System*. Springer Science & Business Media, Sep. 2012.

[9] "Anatomy and Physiology of the Nasal Cavity (Inner Nose) and Mucosa." [Online]. Available: https://www.myvmc.com/medical-centres/lungs-breathing/anatomy-and-physiology-of-the-nasal-cavity-inner-nose-and-mucosa/. Accessed: 2018-03-07

[10] C. Croce, R. Fodil, M. Durand, G. Sbirlea-Apiou, G. Caillibotte, J.-F. Papon, J.-R. Blondeau, A. Coste, D. Isabey, and B. Louis, "In Vitro Experiments and Numerical Simulations of Airflow in Realistic Nasal Airway Geometry," *Annals of Biomedical Engineering*, vol. 34, no. 6, pp. 997–1007, Jun. 2006.

[11] I. Namdar, "What is the role of the nasal septum?" [Online]. Available: https://www.newyorkentspecialist.com/nose/what-is-the-role-of-the-nasal-septum/. Accessed: 2018-04-20

[12] "Septoplasty and Nose Surgery in Sydney." [Online]. Available: http://www.ent-surgery.com.au/nose-and-sinus-surgery/deviated-nasal-septum-septoplasty-surgery/. Accessed: 2018-03-06

[13] B. Y. Ghorayeb, "What is turbinate reduction/turbinectomy?" [Online]. Available: http://www.ghorayeb.com/turbinectomy.html. Accessed: 2018-03-24

[14] M. O. Scheithauer, "Surgery of the turbinates and empty nose syndrome," *GMS Current Topics in Otorhinolaryngology, Head and Neck Surgery*, vol. 9, Apr. 2011.

[15] "Turbinate Anatomy and Physiology." [Online]. Available: http://emptynosesyndrome.org/turbinate-tutorial/turbinate-anatomy-and-physiology. Accessed: 2018-03-19

[16] N. Chhabra and S. M. Houser, "The Diagnosis and Management of Empty Nose Syndrome," *Otolaryngologic Clinics of North America*, vol. 42, no. 2, pp. 311–330, Apr. 2009.

[17] S. M. Houser, "Empty nose syndrome associated with middle turbinate resection," *Otolaryngology-Head and Neck Surgery*, vol. 135, no. 6, pp. 972–973, Dec. 2006.

[18] T. Keck and J. Lindemann, "Numerical simulation and nasal air-conditioning," *GMS Current Topics in Otorhinolaryngology, Head and Neck Surgery*, vol. 9, Apr. 2011.

[19] T. Hildebrandt, L. Goubergrits, W. Heppt, S. Bessler, and S. Zachow, "Evaluation of the Intranasal Flow Field through Computational Fluid Dynamics," *Facial Plastic Surgery*, vol. 29, no. 02, pp. 093–098, Apr. 2013.

[20] J. H. Zhu, H. P. Lee, K. M. Lim, S. J. Lee, L. Teo Li San, and D. Y. Wang, "Inspirational airflow patterns in deviated noses: a numerical study," *Computer Methods in Biomechanics and Biomedical Engineering*, vol. 16, no. 12, pp. 1298–1306, Dec. 2013.

[21] V. N. Riazuddin, M. Zubair, M. Z. Abdullah, R. Ismail, I. L. Shuaib, S. A. Hamid, and K. A. Ahmad, "Numerical study of inspiratory and expiratory flow in a human nasal cavity," *Journal of Medical and Biological Engineering*, vol. 31, no. 3, pp. 201–206, 2011.

[22] C. Li, A. A. Farag, G. Maza, S. McGhee, M. A. Ciccone, B. Deshpande, E. A. Pribitkin, B. A. Otto, and K. Zhao, "Investigation of the abnormal nasal aerodynamics and trigeminal functions among empty nose syndrome patients," *International Forum of Allergy & Rhinology*, 2017.

[23] M.-Y. Di, Z. Jiang, Z.-Q. Gao, Z. Li, Y.-R. An, and W. Lv, "Numerical Simulation of Airflow Fields in Two Typical Nasal Structures of Empty Nose Syndrome: A Computational Fluid Dynamics Study," *PLOS ONE*, vol. 8, no. 12, 2013.

[24] Wexler D, Segal R, and Kimbell J, "Aerodynamic effects of inferior turbinate reduction: Computational fluid dynamics simulation," *Archives of Otolaryngology–Head & Neck Surgery*, vol. 131, no. 12, pp. 1102–1107, Dec. 2005.

[25] Y. S. Cheng, H. C. Yeh, R. A. Guilmette, S. Q. Simpson, K. H. Cheng, and D. L. Swift, "Nasal Deposition of Ultrafine Particles in Human Volunteers and Its Relationship to Airway Geometry," *Aerosol Science and Technology*, vol. 25, no. 3, pp. 274–291, Jan. 1996.

[26] L. Gradon and C. P. Yu, "Diffusional Particle Deposition in the Human Nose and Mouth," *Aerosol Science and Technology*, vol. 11, no. 3, pp. 213–220, Jan. 1989.

[27] K. T. Shanley, P. Zamankhan, G. Ahmadi, P. K. Hopke, and Y.-S. Cheng, "Numerical Simulations Investigating the Regional and Overall Deposition Efficiency of the Human Nasal Cavity," *Inhalation Toxicology*, vol. 20, no. 12, pp. 1093–1100, Jan. 2008.

[28] J. D. Schroeter, J. S. Kimbell, and B. Asgharian, "Analysis of Particle Deposition in the Turbinate and Olfactory Regions Using a Human Nasal Computational Fluid Dynamics Model | Journal of Aerosol Medicine," *Mary Ann Liebert, Inc., publishers*, vol. 19, no. 3, Oct. 2006.

[29] J. Anderson, *Computational Fluid Dynamics: The Basics with Applications*, 8th ed., ser. McGraw-Hill series in mechanical engineering, New York:. McGraw-Hill, 1995.

[30] J. Warnatz, U. Ulrich) Maas, and R. Dibble, *Combustion : physical and chemical fundamentals, modeling and simulation, experiments, pollutant formation / J. Warnatz, U. Maas, R. W. Dibble.*, 4th ed. Springer Science & Business Media, 2006.

[31] CD-adapco, *STAR-CCM+ User Guide for version 12.02.* Siemens PLM Software, 2018.

[32] "What is CFD, Computational Fluid Dynamics?" [Online]. Available: https://www.simscale.com/docs/content/simwiki/cfd/whatiscfd.html. Accessed: 2018-03-16

[33] C. Crowe, J. Schwarzkopf, M. Sommerfeld, and Y. Tsuji, *Multiphase flows with droplets and particles (second edition).* Taylor and Francis Group, CRC Press, 2012.

[34] G. F. Hewitt, "Multiphase flow," in *Thermopedia*, 2011. [Online]. Available: http://www.thermopedia.com/content/4/. Accessed: 2018-04-17

[35] "Turbomachinery CFD." [Online]. Available: https://www.cfdsupport.com/turbomachinery-cfd.html Accessed: 3.05.2018

[36] "Epithelial Tissue - Definition, Types, Function & Examples of Epithelium," Dec. 2016. [Online]. Available: https://biologydictionary.net/epithelial-tissue/. Accessed: 2018-15-05

[37] T. Balasubramanian, "Nasal Resistance its importance and measurement," *ENT Scholar*, vol. 1, no. 3, 2012.

[38] M. Ochs and H. O'Brodovich, "5 - The Structural and Physiologic Basis of Respiratory Disease," in *Kendig & Chernick's Disorders of the Respiratory Tract in Children (Eighth Edition)*, R. W. Wilmott, T. F. Boat, A. Bush, V. Chernick, R. R. Deterding, and F. Ratjen, Eds. Philadelphia: W.B. Saunders, 2012, pp. 35–74.

[39] "Airflow Resistance." [Online]. Available: http://www.pathwaymedicine.org/airflow-resistance. Accessed: 2018-05-02

[40] J. S. J. Haight and P. Cole, "The site and function of the nasal valve," *The Laryngoscope*, vol. 93, no. 1, pp. 49–55, Jan. 2009.

[41] G. S. Kenyon, "Phase variation in nasal airways resistance assessed by active anterior rhinomanometry," *The Journal of Laryngology & Otology*, vol. 101, no. 09, pp. 910–916, Sep. 1987.

[42] L. Viani, A. S. Jones, and R. Clarke, "Nasal airflow in inspiration and expiration," *The Journal of Laryngology & Otology*, vol. 104, no. 06, pp. 473–476, Jun. 1990.

[43] I. Hörschler, M. Meinke, and W. Schröder, "Numerical simulation of the flow field in a model of the nasal cavity," *Computers & Fluids*, vol. 32, no. 1, pp. 39–45, 2003.

[44] J. H. Zhu, H. P. Lee, K. M. Lim, S. J. Lee, and D. Y. Wang, "Evaluation and comparison of nasal airway flow patterns among three subjects from Caucasian, Chinese and Indian ethnic groups using computational fluid dynamics simulation," *Respiratory Physiology & Neurobiology*, vol. 175, no. 1, pp. 62–69, Jan. 2011.

[45] W. McCabe, J. C. Smith, and P. Harriott, *Unit Operations of Chemical Engineering.*, 7th ed. Boston, Mass.:: McGraw-Hill Higher Eduacation, 2005.

[46] J. Sozansky and S. M. Houser, "Pathophysiology of empty nose syndrome: Pathophysiology of Empty Nose Syndrome," *The Laryngoscope*, vol. 125, no. 1, pp. 70–74, Jan. 2015.

[47] M. Lippmann, "Deposition and clearance of inhaled particles in the human nose," *Annals of Otology, Rhinology & Laryngology*, vol. 79, no. 3, pp. 519–528, 1970.

[48] G. J. Garcia, E. W. Tewksbury, B. A. Wong, and J. S. Kimbell, "Interindividual Variability in Nasal Filtration as a Function of Nasal Cavity Geometry," *Journal of Aerosol Medicine and Pulmonary Drug Delivery; New Rochelle*, vol. 22, no. 2, pp. 139–55, Jun. 2009.

[49] "Interventions for atrophic rhinitis | Cochrane." [Online]. Available: http://www.cochrane.org/CD008280/ENT_interventions-for-atrophic-rhinitis. Accessed: 2018-05-05

[50] J. N. Baraniuk and D. Kim, "Nasonasal reflexes, the nasal cycle, and sneeze," *Current allergy and asthma reports*, vol. 7, no. 2, pp. 105–111, 2007.

Appendix A

Additional results: Cross-sectional area

At first, the cross-sectional area (CSA) for all geometries along the nasal cavity at each coronal from the nostrils to the nasopharynx was calculated in STAR-CCM+, shown in Figure A.1. Further, the CSA for the right and left nasal cavity in each model is presented.

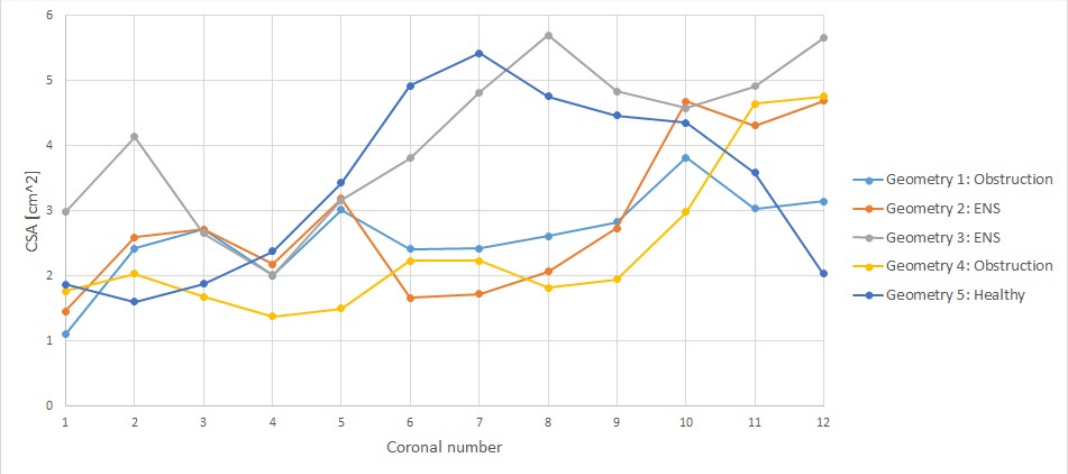

Figure A.1: Cross-sectional area to all the geometries along the coronal direction.

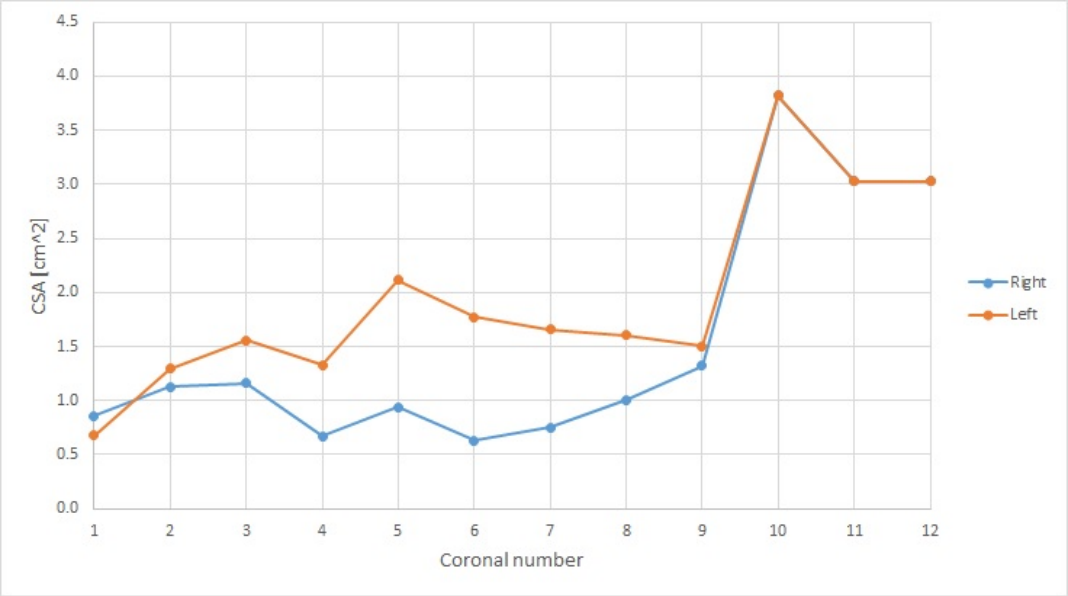

Figure A.2: Cross-sectional area in the right and left nasal cavity for geometry 1.

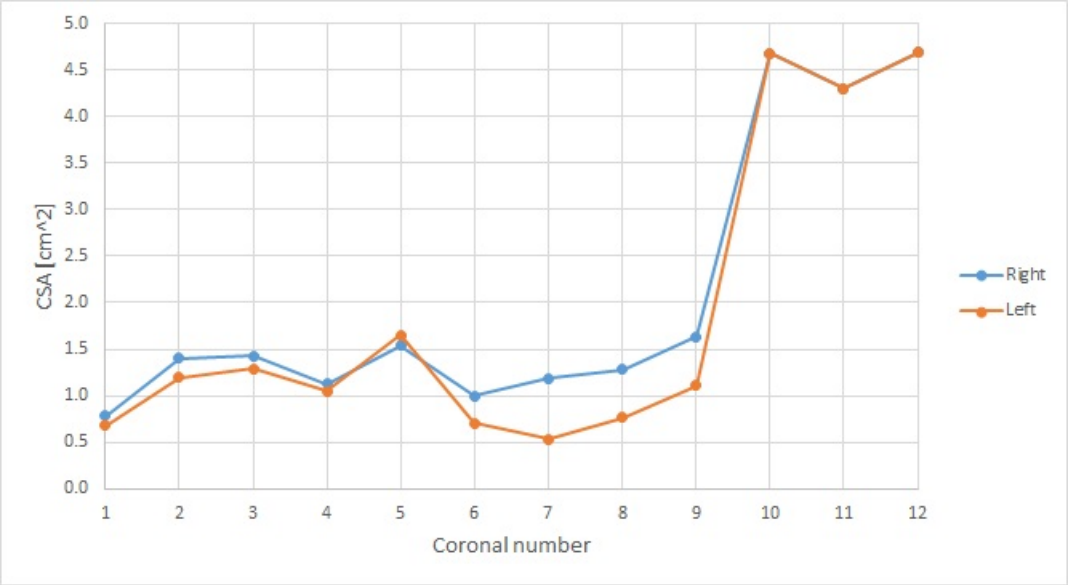

Figure A.3: Cross-sectional area in the right and left nasal cavity for geometry 2.

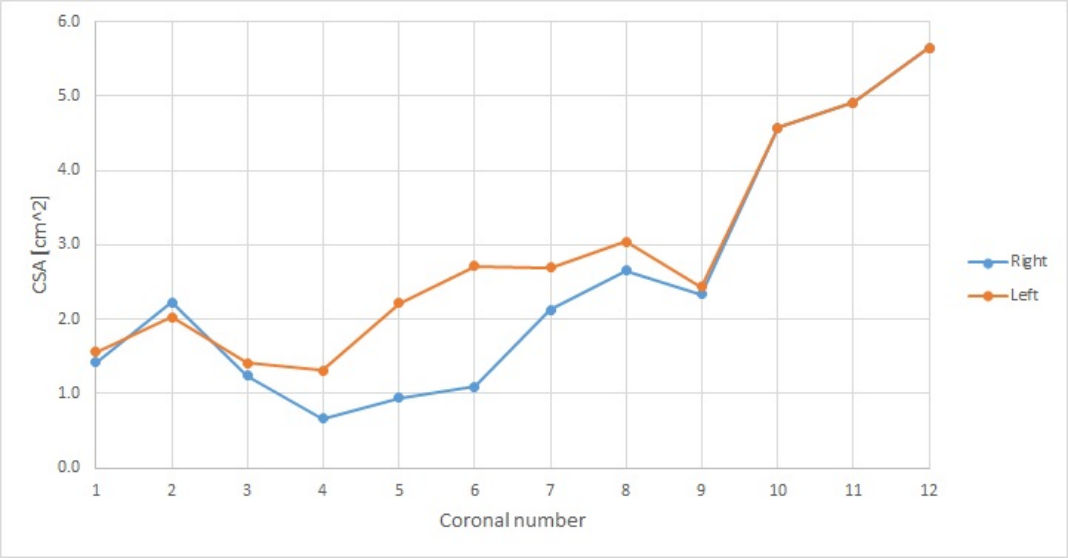

Figure A.4: Cross-sectional area in the right and left nasal cavity for geometry 3.

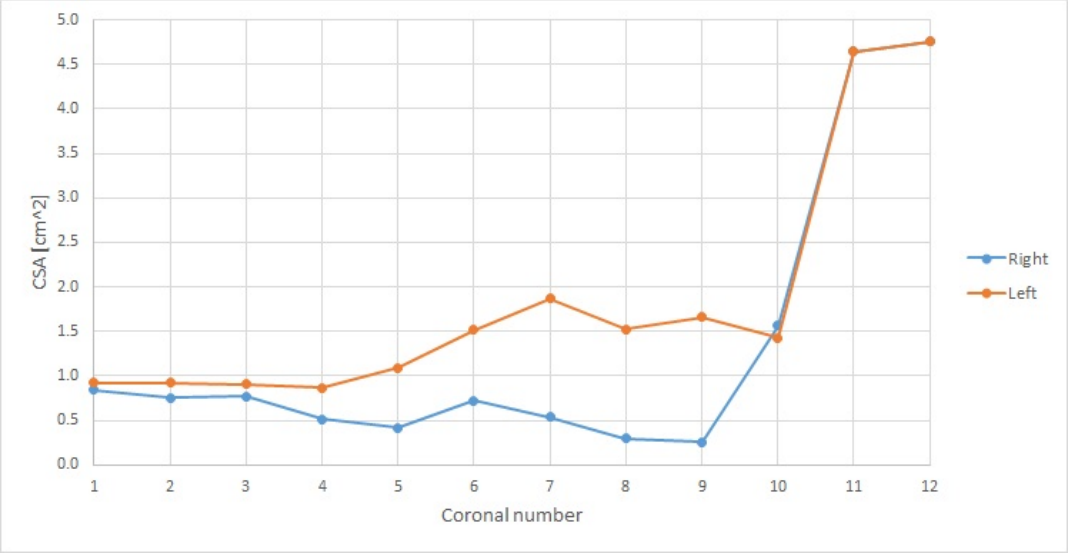

Figure A.5: Cross-sectional area in the right and left nasal cavity for geometry 4.

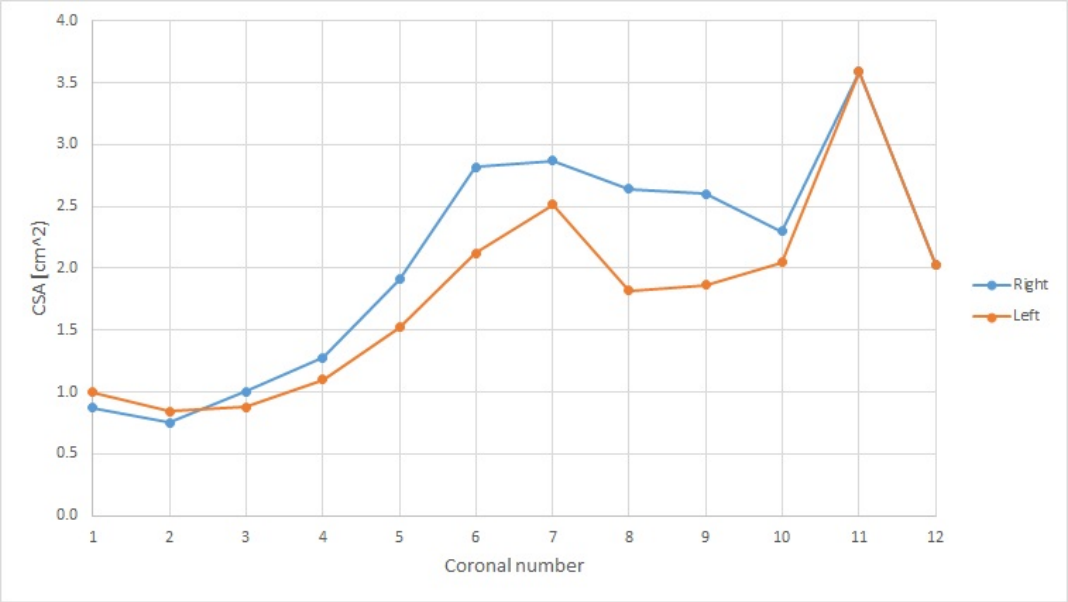

Figure A.6: Cross-sectional area in the right and left nasal cavity for geometry 5.

Appendix B

Additional results: Pressure distribution on the right and left side of the nasal cavity

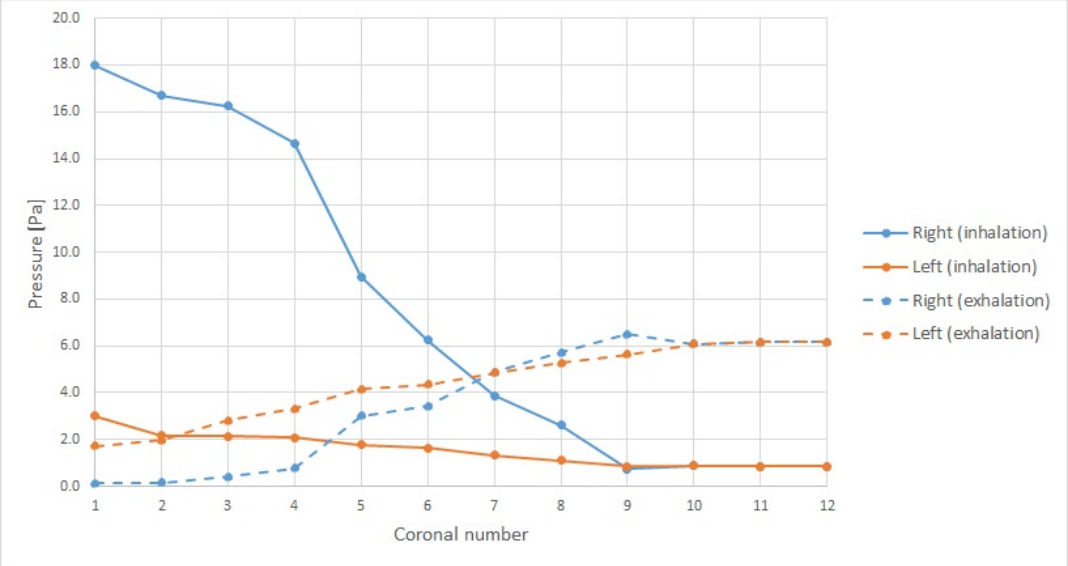

Figure B.1: Pressure distribution in the right and left nasal cavity for geometry 1. Coronal 1 is nearest the nostrils and coronal number 12 is at the nasopharynx.

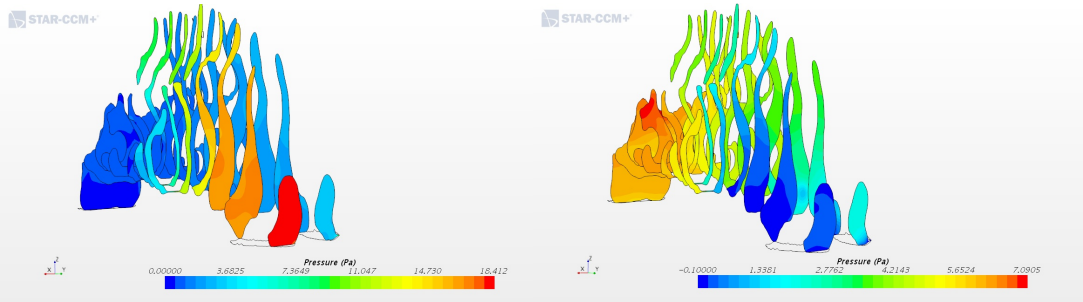

(a) Inhalation. **(b)** Exhalation.

Figure B.2: Pressure distribution in the nasal cavity for geometry 1 at inhalation and exhalation.

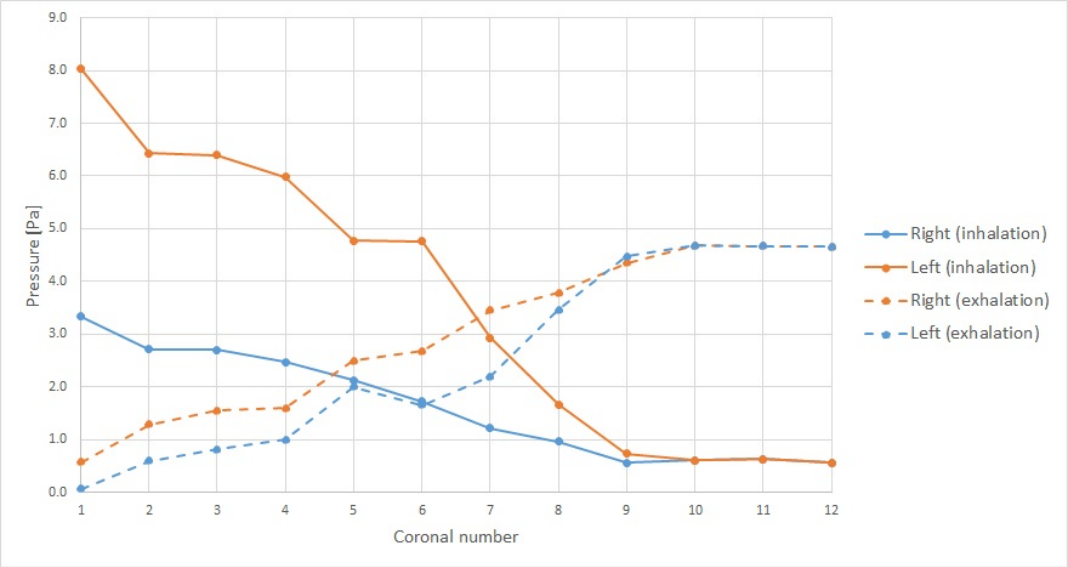

Figure B.3: Pressure distribution in the right and left nasal cavity for geometry 2. Coronal 1 is nearest the nostrils and coronal number 12 is at the nasopharynx.

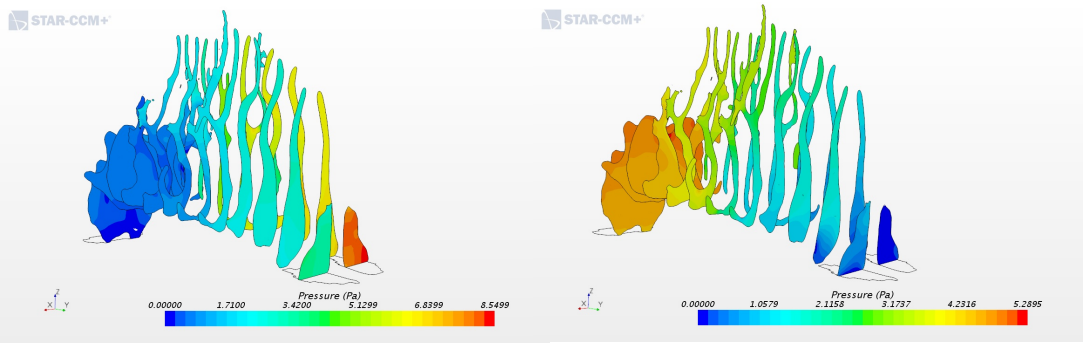

(a) Inhalation. **(b)** Exhalation.

Figure B.4: Pressure distribution in the nasal cavity for geometry 2 at inhalation and exhalation.

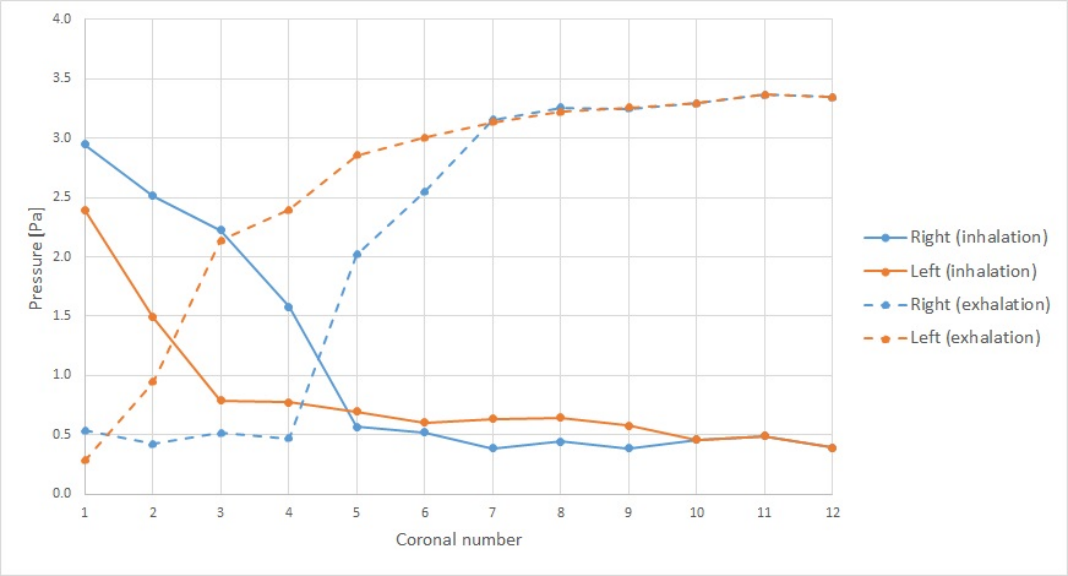

Figure B.5: Pressure distribution in the right and left nasal cavity for geometry 3. Coronal 1 is nearest the nostrils and coronal number 12 is at the nasopharynx.

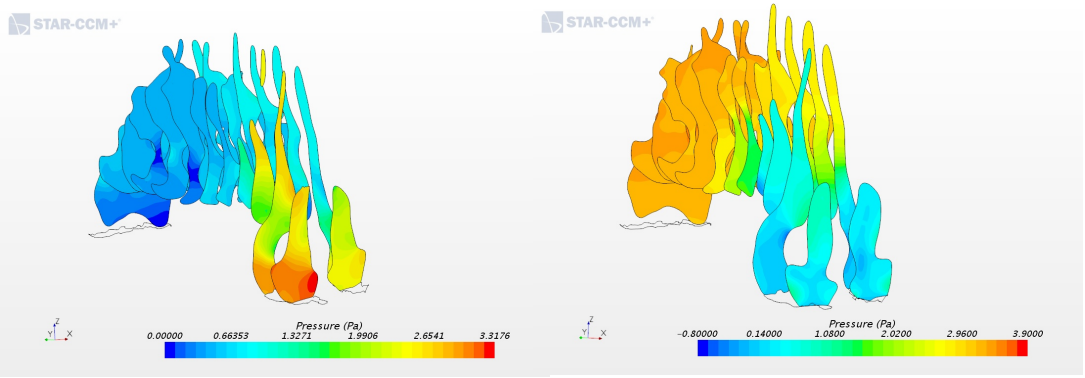

(a) Inhalation. **(b)** Exhalation.

Figure B.6: Pressure distribution in the nasal cavity for geometry 3 at inhalation and exhalation.

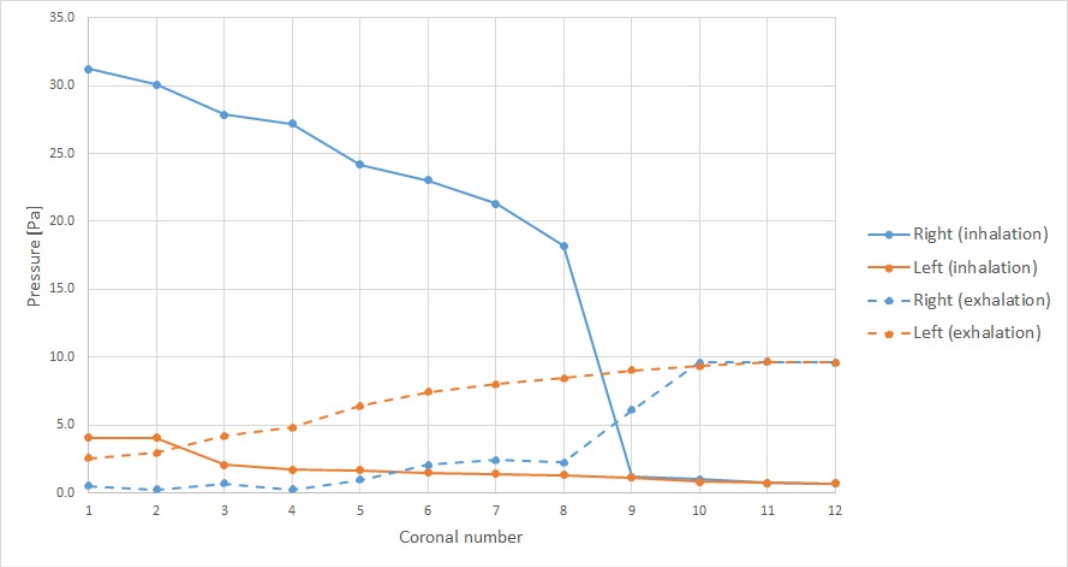

Figure B.7: Pressure distribution in the right and left nasal cavity for geometry 4. Coronal 1 is nearest the nostrils and coronal number 12 is at the nasopharynx.

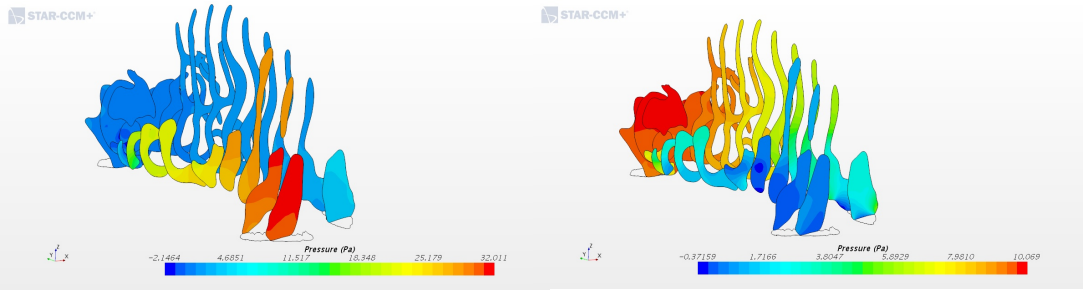

(a) Inhalation. **(b)** Exhalation.

Figure B.8: Pressure distribution in the nasal cavity for geometry 4 at inhalation and exhalation.

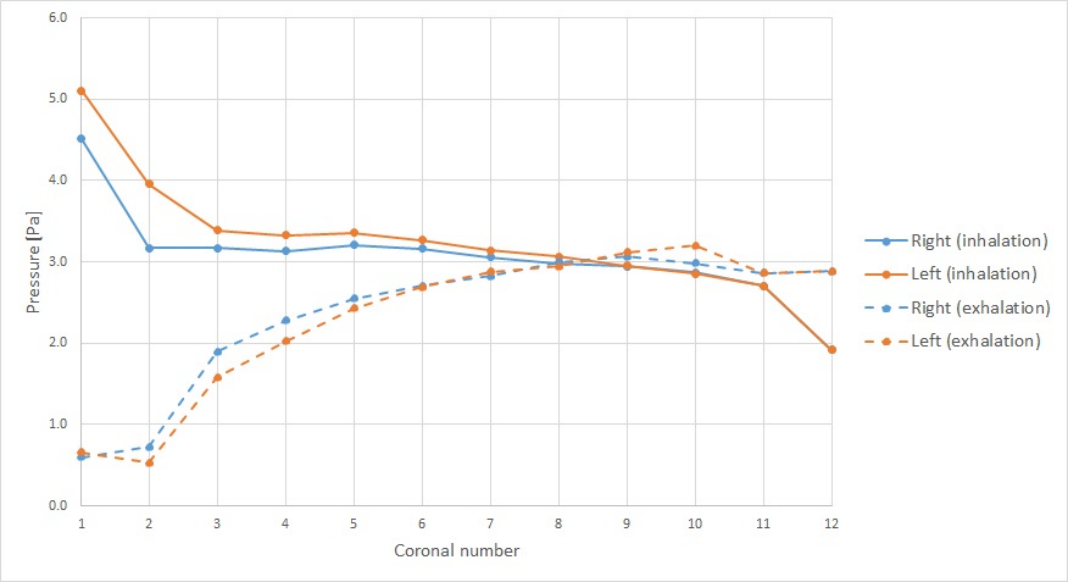

Figure B.9: Pressure distribution in the right and left nasal cavity for geometry 5. Coronal 1 is nearest the nostrils and coronal number 12 is at the nasopharynx.

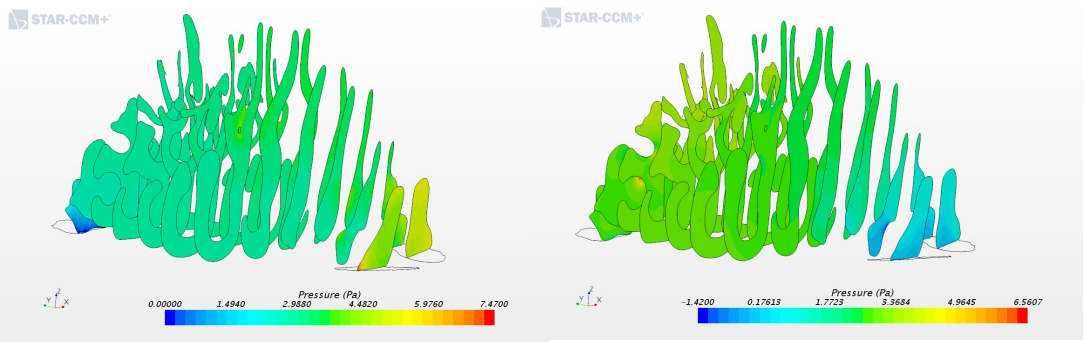

(a) Inhalation. **(b)** Exhalation.

Figure B.10: Pressure distribution in the nasal cavity for geometry 5 at inhalation and exhalation.

Appendix C

Nasal cavity divided into 3 regions: anterior, IT and MT

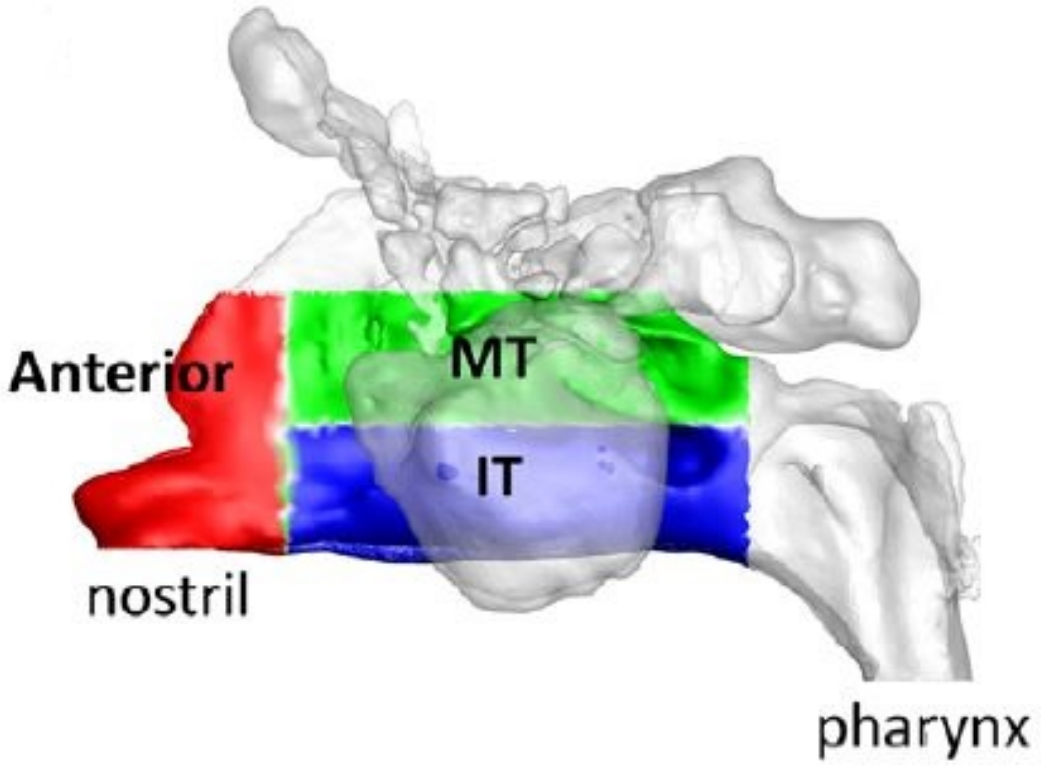

Figure C.1: Overview of the nasal cavity divided into 3 regions: anterior, IT and MT [22].

Appendix D

Additional results: Streamline patterns in the nasal cavity

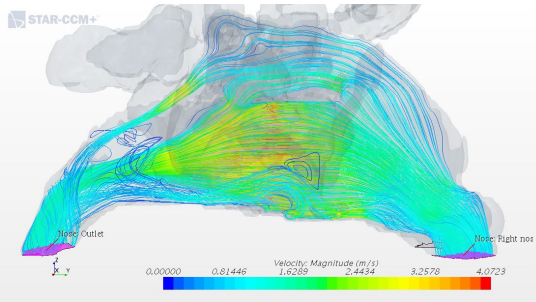

(a) Inhalation: streamlines from the right nostril.

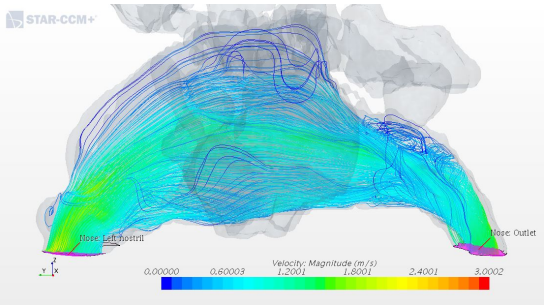

(b) Inhalation: streamlines from the left nostril.

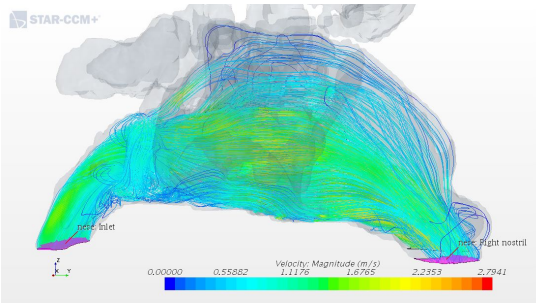

(c) Exhalation: streamlines from the nasopharynx and out the right nostril.

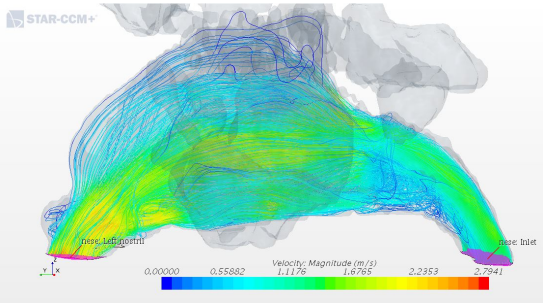

(d) Exhalation: streamlines from the nasopharynx and out the left nostril.

Figure D.1: Airflow patterns for geometry 1, displayed by streamlines at inhalation and exhalation.

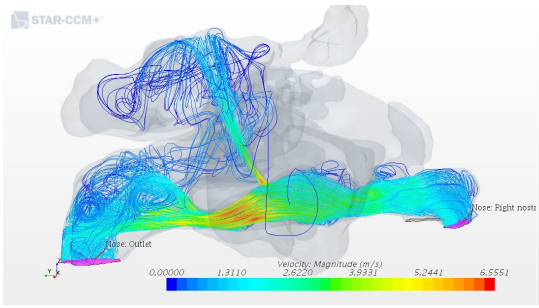

(a) Inhalation: streamlines from the right nostril.

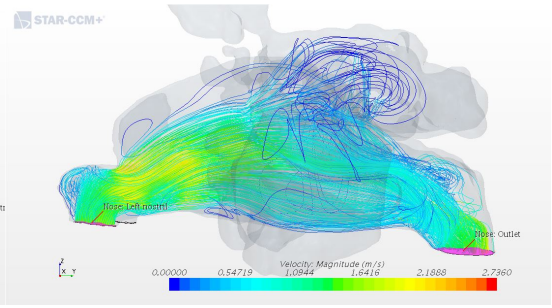

(b) Inhalation: streamlines from the left nostril.

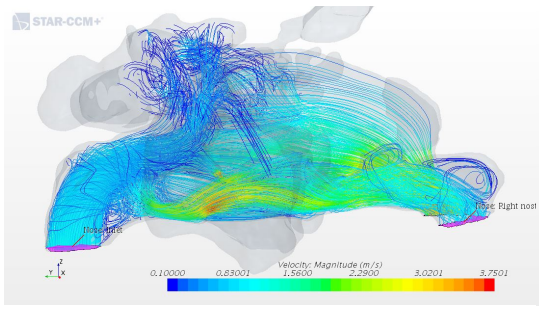

(c) Exhalation: streamlines from the nasopharynx and out the right nostril.

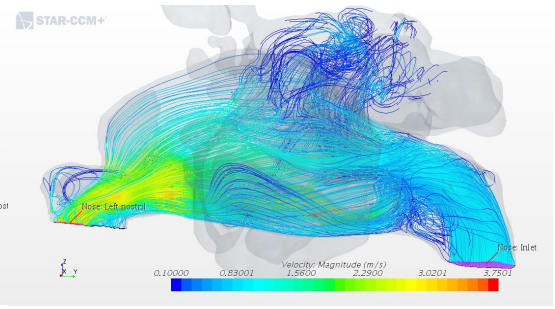

(d) Exhalation: streamlines from the nasopharynx and out the left nostril.

Figure D.2: Airflow patterns for geometry 4, displayed by streamlines at inhalation and exhalation.

Appendix E

Additional results: Velocity distribution in the nostrils

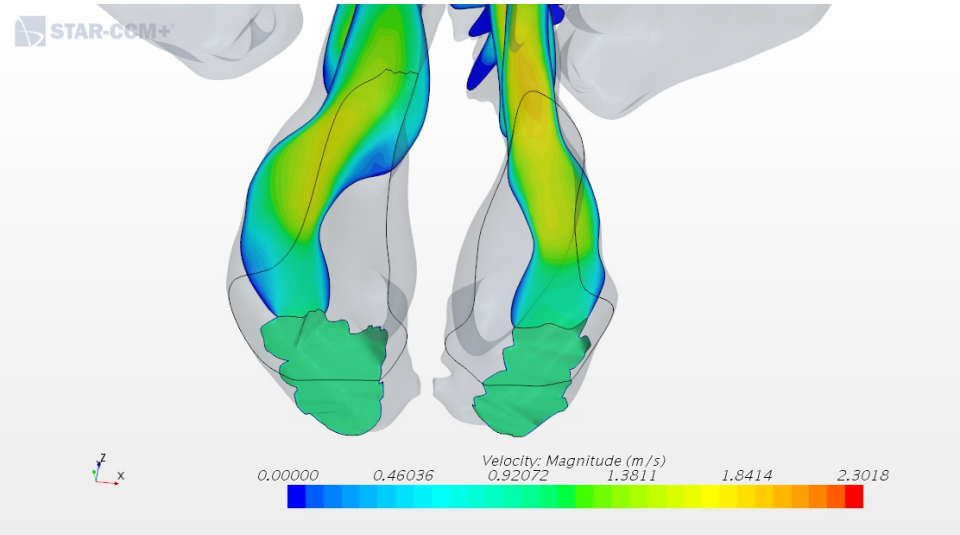

(a) Innhalation.

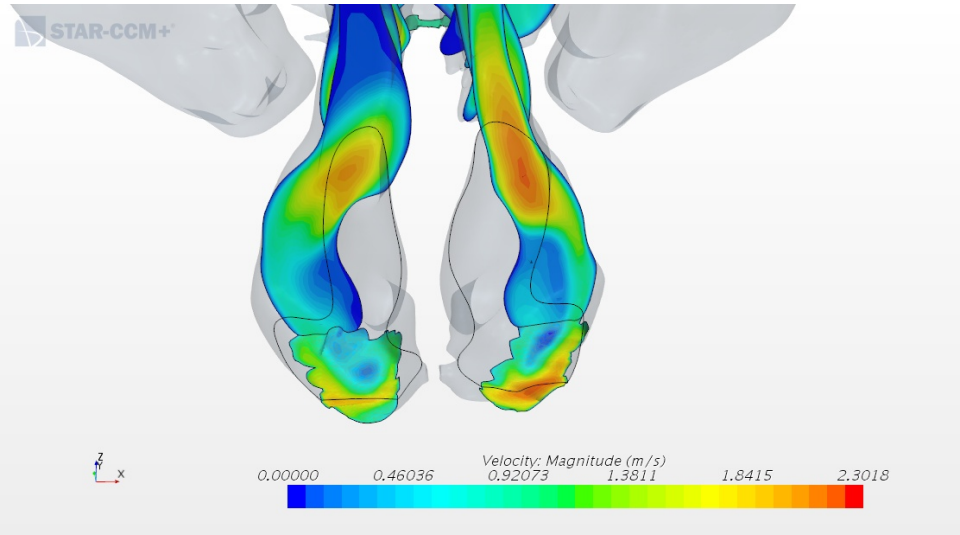

(b) Exhalation.

Figure E.1: Velocity distribution in the nostrils for geometry 3 at inhalation and exhalation.

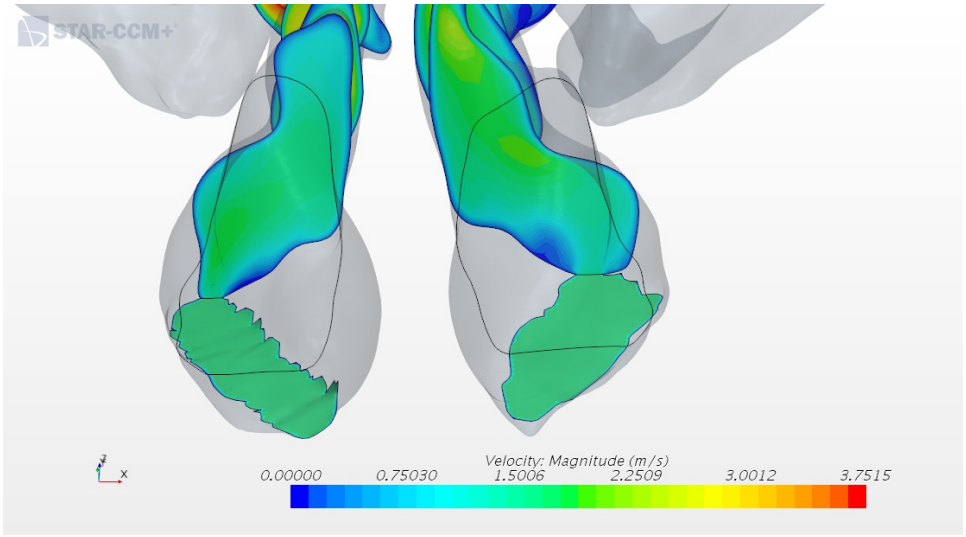

(a) Innhalation.

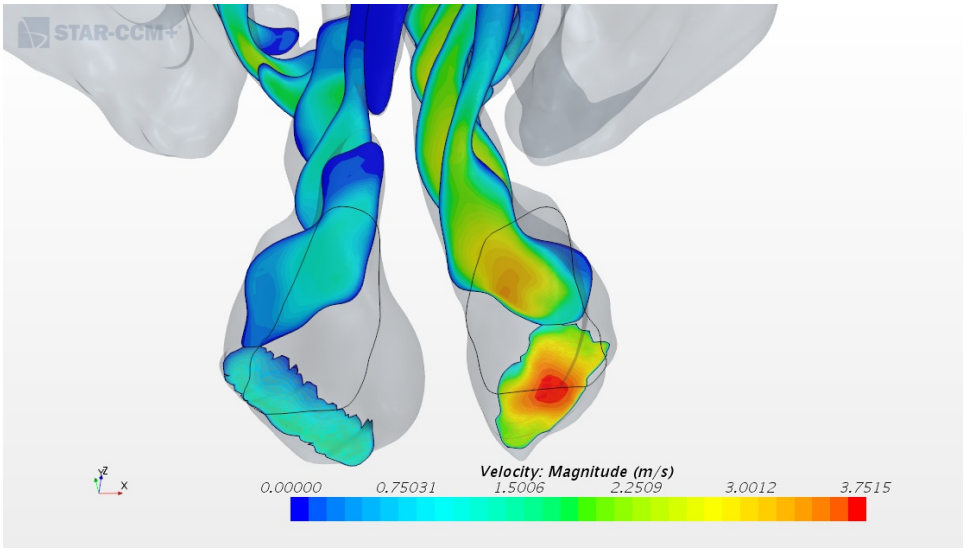

(b) Exhalation.

Figure E.2: Velocity distribution in the nostrils for geometry 4 at inhalation and exhalation.

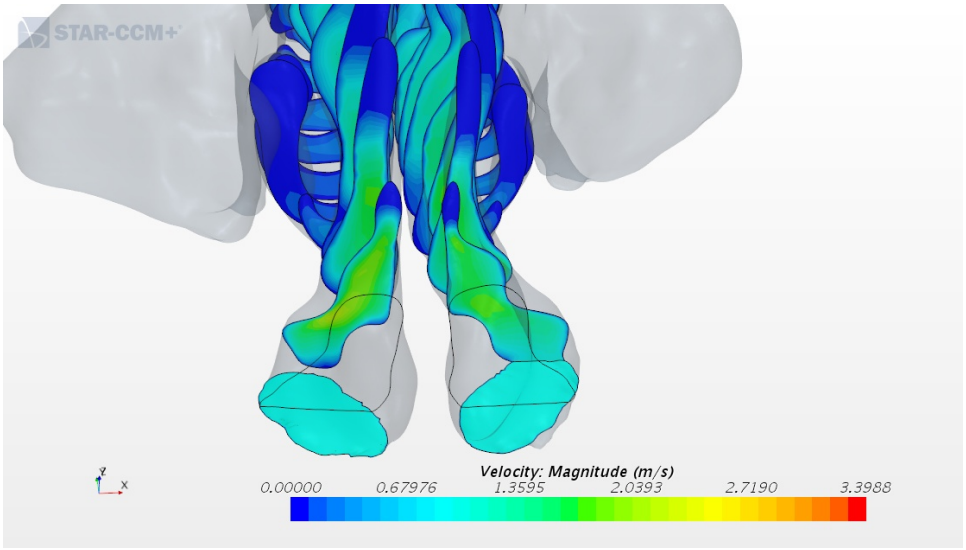

(a) Innhalation.

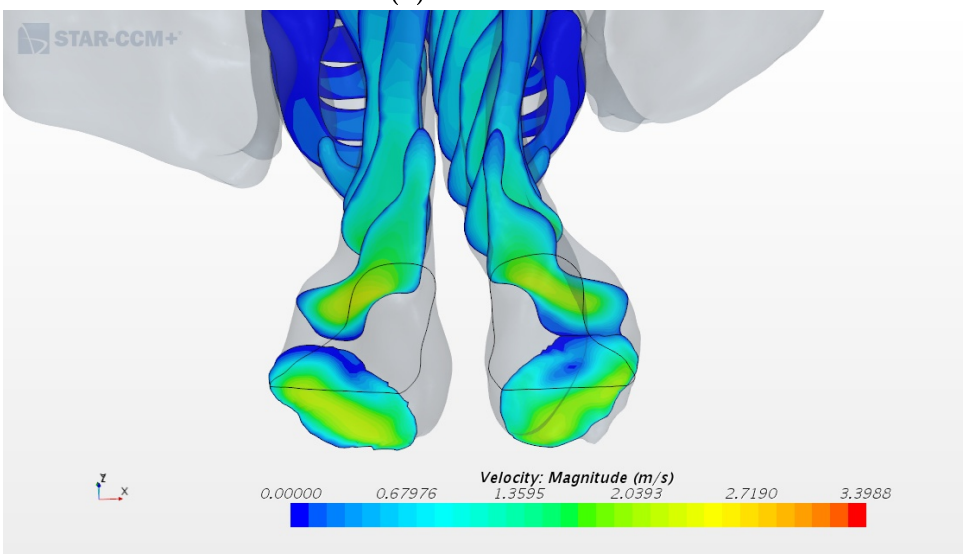

(b) Exhalation.

Figure E.3: Velocity distribution in the nostrils for geometry 5 at inhalation and exhalation.

Appendix F

Additional results: Particle deposition

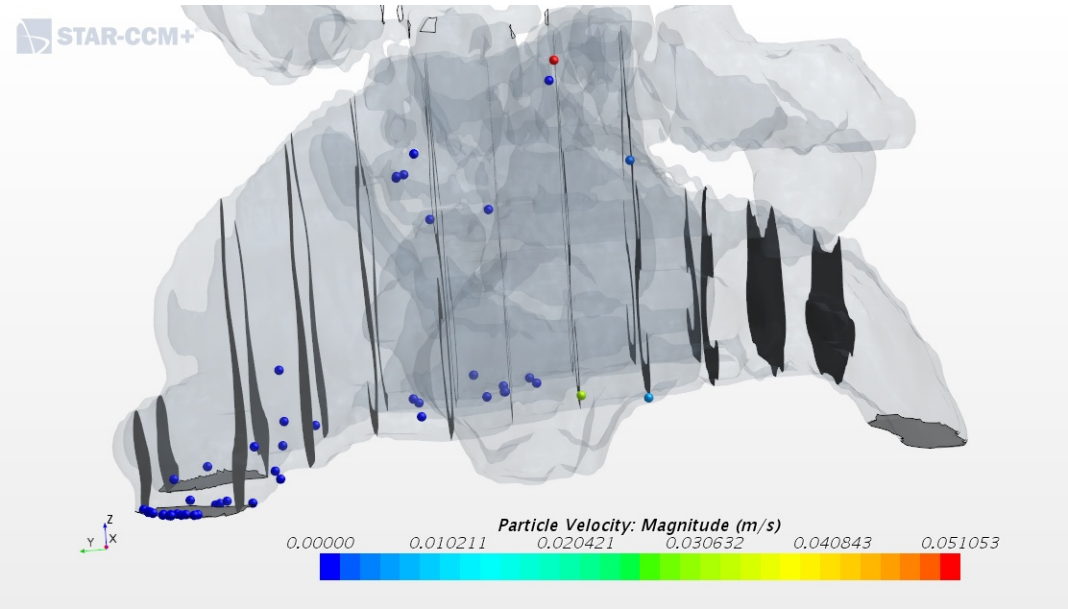

Figure F.1: Particle deposition in the nasal cavity for geometry 1.

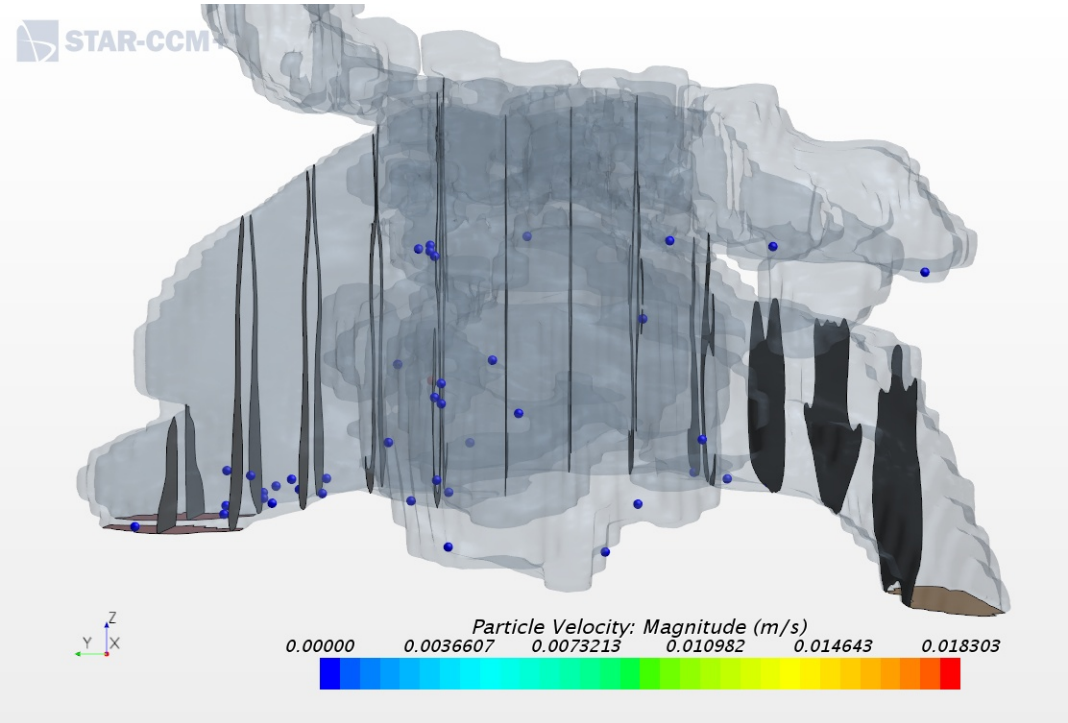

Figure F.2: Particle deposition in the nasal cavity for geometry 2.

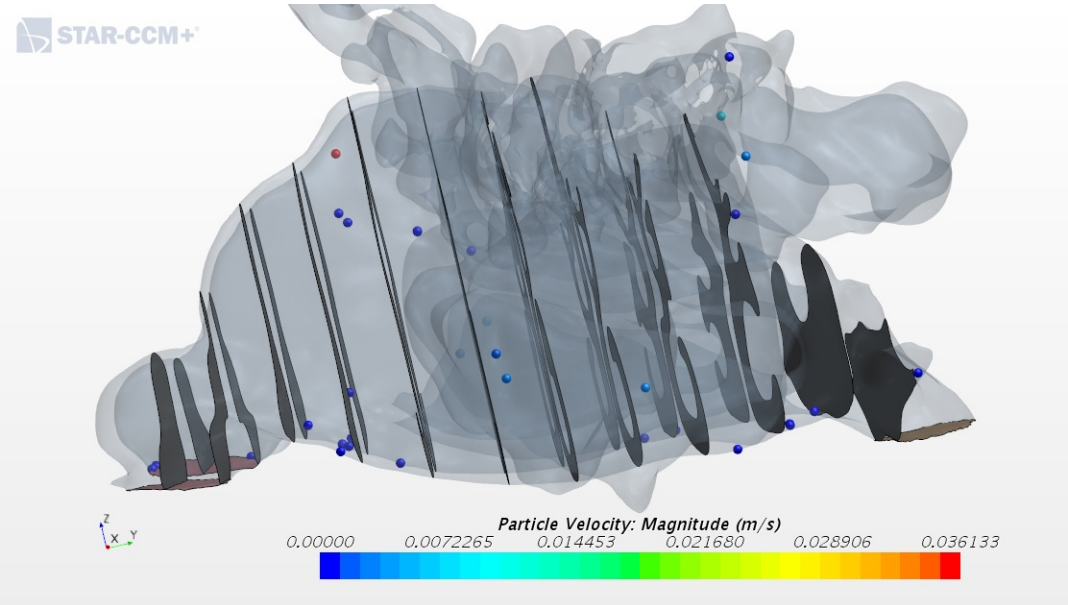

Figure F.3: Particle deposition in the nasal cavity for geometry 5.